

Ultrasonic Imaging of the Onset and Growth of Fractures Within Partially Saturated Whitby Mudstone Using Coda Wave Decorrelation Inversion

Zotz-Wilson, Reuben; Douma, Lisanne A.N.R.; Sarout, Joel; Dautriat, Jeremie; Dewhurst, David; Barnhoorn, Auke

DOI

[10.1029/2020JB020042](https://doi.org/10.1029/2020JB020042)

Publication date

2020

Document Version

Final published version

Published in

Journal of Geophysical Research: Solid Earth

Citation (APA)

Zotz-Wilson, R., Douma, L. A. N. R., Sarout, J., Dautriat, J., Dewhurst, D., & Barnhoorn, A. (2020). Ultrasonic Imaging of the Onset and Growth of Fractures Within Partially Saturated Whitby Mudstone Using Coda Wave Decorrelation Inversion. *Journal of Geophysical Research: Solid Earth*, 125(7), Article e2020JB020042. <https://doi.org/10.1029/2020JB020042>

Important note

To cite this publication, please use the final published version (if applicable). Please check the document version above.

Copyright

Other than for strictly personal use, it is not permitted to download, forward or distribute the text or part of it, without the consent of the author(s) and/or copyright holder(s), unless the work is under an open content license such as Creative Commons.

Takedown policy

Please contact us and provide details if you believe this document breaches copyrights. We will remove access to the work immediately and investigate your claim.

Ultrasonic Imaging of the Onset and Growth of Fractures Within Partially Saturated Whitby Mudstone Using Coda Wave Decorrelation Inversion

Reuben Zotz-Wilson¹ , Lisanne A. N. R. Douma¹, Joel Sarout² , Jeremie Dautriat², David Dewhurst² , and Auke Barnhoorn¹ 

¹Faculty of Civil Engineering and Geoscience, Delft University of Technology, Delft, Netherlands, ²CSIRO-Energy, Perth, Western Australia, Australia

Key Points:

- Inversion of coda wave decorrelation data allows the imaging of subwavelength strain localization
- CWD inversion is capable of imaging aseismic triaxial deformation and failure of the Whitby mudstone
- Onset of aseismic precursory strain is imaged at less than 42% of peak differential stress

Supporting Information:

- Supporting Information S1

Correspondence to:

R. Zotz-Wilson,
rdzotz@gmail.com

Citation:

Zotz-Wilson, R., Douma, L. A. N. R., Sarout, J., Dautriat, J., Dewhurst, D., & Barnhoorn, A. (2020). Ultrasonic imaging of the onset and growth of fractures within partially saturated Whitby Mudstone using coda wave decorrelation inversion. *Journal of Geophysical Research: Solid Earth*, 125, e2020JB020042. <https://doi.org/10.1029/2020JB020042>

Received 24 APR 2020

Accepted 12 JUN 2020

Accepted article online 15 JUN 2020

Abstract Using active ultrasonic source survey data, coda wave decorrelation (CWD) time-lapse imaging during the triaxial compression of Whitby Mudstone cores provides a 3-D description of the evolution and redistribution of inelastic strain concentrations. Acoustic emissions (AEs) monitoring is also performed between any two consecutive surveys. From these data, we investigate the impact of initial water saturation S_w on the onset, growth, and reactivation of inelastic deformation, compared to the postdeformation fracture network extracted from X-ray tomography scans. Our results indicate for the applied strain rate and degree of initial water saturation, and within the frequency range of our ultrasonic transducers (0.1 to 1 MHz), that inelastic strain localization and propagation in the Whitby Mudstone does not radiate AEs of sufficient magnitude to be detected above the average noise level. This is true for both the initial onset of inelasticity (strain localization) and during macroscopic failure. In contrast, the CWD results indicate the onset of what is interpreted as localized regions of inelastic strain at less than 50% of the peak differential stress the Whitby Mudstone can sustain. The seemingly aseismic nature of these clay-rich rocks suggests the gradual development of inelastic strain, from the microscopic diffuse damage, up until the macroscopic shear failure.

1. Introduction

Mudstones play an important role in civil infrastructure, energy, and resource projects globally. They act as impermeable seals in conventional hydrocarbon or sequestration capture reservoirs (Armitage et al., 2016; Busch et al., 2008) or as both a source (Jianghui et al., 2012) and reservoir rock (Aplin & Macquaker, 2011) in unconventional hydrocarbon projects. Several permanent nuclear storage projects plan to (Brookins, 1976; Vomvoris et al., 2013) or already employ (Aik & Sundell, 2014) mudstones as the host rock for both high- and low-grade radioactive waste. Due to their global abundance (Garrels & Mackenzie, 1969), civil infrastructure projects such as tunnels, dams, and bridges often directly interact with mudstones (Izumi et al., 1998; Yoshida et al., 1997; Wang et al., 2013), presenting a variety of engineering challenges. Furthermore, the presence of shales and mudstones is an important input to susceptibility maps for environmental damage due to landslides (Ayalew & Yamagishi, 2005). It is therefore essential to gain an understanding of the mechanical properties of mudstones under a variety of environmental conditions. To this end, laboratory triaxial testing of core samples subjected to realistic subsurface temperature, pressure, stress, and saturation conditions are essential.

While the bulk core properties are generally attainable by measurements at the boundary of the sample, the determination of the time and location at which inelastic changes develop, requires techniques which are sensitive to localized changes within the core. Acoustic emissions (AEs) monitoring has been a commonly applied technique within rock-mechanics laboratories for more than four decades (Heap et al., 2009; Lei et al., 2004; Lockner, 1993; Lockner et al., 1977; Sarout et al., 2017), enabling the rate, location, and effective stress at which fracturing develops to be extracted from passive acoustic monitoring. Some inherent limitations of AEs monitoring are that it requires (i) the magnitude of acoustic energy emitted during fracturing to be sufficiently large, and (ii) within the dynamic range that it is detectable by the available sensor network. Further, AEs monitoring is unable to detect inelastic changes which are truly aseismic in nature (Main, 1990). The term scatterer/s is used throughout this manuscript to describe any localized contrast in density/velocity of

size in the order of the probing wavefields dominant wavelength. In the context of the current study, a region of localized microfractures, a larger macroscopic fracture, mineral impurities, voids, or the layered mudstone structure can all be considered as wavefield scatterers.

In this study, we apply both active source acoustic and passive AEs monitoring, on three laboratory scale core samples of different initial water saturation. The aim is to monitor both the location and time of fracturing from active source monitoring, in comparison with the onset of AEs, thereby indicating the degree to which preseismic changes occur. This is based on the premise that active source methods do not rely on the spontaneous emission of acoustic energy in order to detect the presence of inelastic deformation, and therefore remain, in principle, sensitive to aseismic fracturing. While there have been several velocity tomography monitoring applications in laboratory rock deformation experiments (Aben et al., 2019; Brantut, 2018; Jansen et al., 1993), enabling the three-dimensional imaging of rock fracturing, in this work we apply coda wave decorrelation (CWD) inversion for the first time within experimental rock mechanics. The CWD method can be classed as a coda wave interferometric method, which in the most general terms infers subtle changes in medium properties by analyzing changes in the coda wave. This concept under the name coda wave interferometry (CWI) has been shown to display improved sensitivity to perturbations in velocity when compared to changes derived from first arrivals (wave onset) (Grêt, 2005; Snieder, 2002; Zotz-Wilson, Boerrigter, et al., 2019). This is explicitly discussed in terms of experimental rock mechanics in the recent work by Singh et al. (2019) where CWI is performed on synthetic waveforms derived from numerically simulated wave propagation in heterogeneous rock samples. It should be noted that while CWI is often used to describe changes in velocity at the macro (civil structures) (Griffiths et al., 2018; Salvermoser et al., 2015; Zhang et al., 2013, 2016) and mesoscale (seismological systems, volcanoes, reservoirs) (Grêt, 2005; Grêt et al., 2006a; Sens-Schönfelder & Larose, 2008; Sens-Schönfelder & Wegler, 2006; Snieder & Hagerty, 2004), its initial formulation presented the ability to also infer changes in source location and the average displacement of scatterers (Snieder, 2002). In this context CWD can be considered as a CWI technique where the focus is on changes in the scattering properties of a medium, such as that associated with the formation of fractures, or the opening/closure/slip of in situ fractures. While CWI has been applied in several studies to track changes in the source location (Robinson, Sambridge, et al., 2007; Robinson, Snieder, et al., 2007; Zhan et al., 2020) there are few application of its ability to monitor bulk changes in scatterers (Singh et al., 2019; Zotz-Wilson, Boerrigter, et al., 2019). The first publication and experimental application of what we refer to as CWD inversion demonstrated the ability to locate, in a probabilistic sense, the formation of a single defect within a concrete slab by active source time-lapse measurements from several ultrasonic receivers (Larose et al., 2010). Since this initial publication, other works have applied CWD inversion to monitor the formation of cracks in concrete structures (Larose et al., 2015; Zhang et al., 2016), or study changes due to volcanic (Obermann et al., 2013) or tectonic (Obermann et al., 2014, 2019) activity. In this study we apply a modified least squares approach which has the potential to locate, in terms of a material's scattering properties, multiple regions of change simultaneously (Planès et al., 2015).

The results of this study, monitoring the active and passive acoustic response of mudstone samples of differing initial water saturation, provides valuable information on the development of both microscopic inelastic strain (diffuse damage) and the emergence of larger coalesced macroscopic shear fractures.

2. Materials and Methods

2.1. Sample Material and Preparation

The mudstone samples originate from the outcropping Whitby Mudstone formation (WMF), United Kingdom (UK). The WMF is deposited in the East English Cleveland Basin in anoxic bottom conditions (Powell, 2010). This Toarcian Age mudstone formation consists of three members, including the Gray Shale Member, Mulgrave Shale Member, and Alum Shale Member (Powell, 2010). The Mulgrave Shale Member (Lower Jurassic) is the lateral equivalent of the Dutch Posidonia Shale Formation (PSF), the main shale gas target in the Netherlands. The maximum burial depth of the mudstones in the Cleveland Basin is ~4 km, where the top of the Lower Jurassic does not exceed ~2.5 km (Pye, 1985). The WMF has been considered an analog for the Dutch PSF (Zijp et al., 2015), since the PSF is not outcropping in the Netherlands, core material is badly preserved, and available log data is limited.

The WMF is a relatively clay-rich rock, composed of 50% to 70% interlayered illite/smectite, illite, and kaolinite (Houben, Barnhoorn, Wasch, et al., 2016). The organic matter (TOC ~6%) is often interlayered within the matrix (Houben, Barnhoorn, Wasch, et al., 2016; Zijp et al., 2015). The porosity of the mudstones originating from the Mulgrave Shale Member is ~13%, based on the wet and dry mass of a mudstone core (Douma et al., 2019). The matrix permeability is in the range of 10×10^{-23} to 10^{-18} m² as estimated by Houben, Barnhoorn, Lie-A-Fat, et al. (2016) via the Kozeny-Carman equation relating matrix permeability to the porosity determined from He pycnometry and the pore surface area from gas adsorption, where average matrix grain size is 0.1 to 2 μm. The pore diameters were obtained from scanning electron microscope mosaics resulting in a distribution between 72 and 300 nm.

Mudstone blocks were sampled from a wave cut platform on the east coast of England, north of Whitby (UK), near Runswick Bay. The mudstones in the outcrop are submerged daily by seawater, due to the tidal cycle. Immediately after sampling, the mudstone blocks were stored in seawater to prevent initial pore water loss. Seawater was used under the assumption that the pore fluid of the mudstones reached chemical equilibrium with the seawater over geological time.

Cylindrical core plugs were cored normal to the bedding out of the same larger sample block and have a length of ~80 mm and a diameter of ~38 mm. During coring, seawater was used as the cooling fluid to prevent drying, shrinkage or swelling of the clays. The ends of the sample were then trimmed and ground using a fine diamond facing wheel and a precision V-block on a magnetic base, such that the perpendicularity of the end surface to circumferential surface and flatness of the end surfaces are within the general tolerances recommended by the International Society for Rock Mechanics. The preserved core plugs were imaged with an X-ray computed tomography scanner to ensure no major bedding parallel fractures were created during the coring and grinding process.

After coring, the core plugs were stored at room temperature in three different desiccators with a constant relative humidity atmosphere of ~85%, 75%, and 35%. At these relative humidities, the corresponding water saturations achieved after several weeks (until mass stabilization) are $\sim 70 \pm 10\%$, $\sim 58 \pm 10\%$, and $\sim 28 \pm 10\%$, obtained by the method of oversaturated brines as described in detail by Laloui et al. (2013).

The porosity was calculated from a pulverized disk taken from the same mudstone block as all core samples, which was vacuum dried for 24 hr at 105°C, and analyzed with a pycnometer-(He) to determine the grain density ρ_{grain} . This process was repeated 10 times to determine the final ρ_{grain} . The bulk density ρ_{bulk} was calculated using the bulk volume V_{bulk} before drying and the dry mass m_{dry} of the mudstone disk, measured after drying under vacuum in an oven at 105°C until mass stabilization was achieved (Douma et al., 2019). Smectite desiccation in general leads to shrinkage of the clay minerals—meaning that the bulk volume might change due to drying. Further, open fractures will form due to drying, which will also affect the bulk volume of the core plug. Therefore, we have chosen to use the bulk volume of the initial sample V_{bulk} before drying. The obtained porosity φ was cross-checked with that estimated from the water content. The water content was measured by weighing the mudstone disk in the saturated state (i.e., pore fluids preserved as recovered), followed by drying in a vacuum oven at 105°C until mass stabilization, and remeasuring the dry weight (Dewhurst et al., 2015; Douma et al., 2019). The resulting bulk material properties of the sample block are porosity of ~13%; dry bulk grain density of ~ 2.35 g cm⁻³; average grain density from 2.65 to 2.72 g cm⁻³. After the three core plugs were deemed equilibrated in their respective desiccator (approximately 2 months), each rock sample was triaxially deformed, with time-lapse active and passive ultrasonic monitoring.

2.2. Experimental Procedure

The triaxial stress vessel used for the deformation experiments with time lapse ultrasonic monitoring was located in CSIRO's Geomechanics & Geophysics Laboratory in Perth, Australia (Douma et al., 2019; Sarout et al., 2015, 2017). The partially saturated core plugs are placed in a Viton sleeve to prevent contact with the surrounding confining oil. Two diametrically opposed linear variable differential transformers (LVDTs) are mounted within the pressure vessel, as close as possible to the sample in order to monitor the average axial displacement between the two end faces of the cylindrical shale sample. The local radial strain is measured with a two-point strain gauge-based cantilever mounted through the Viton sleeve, directly on the lateral surface of the core plug.

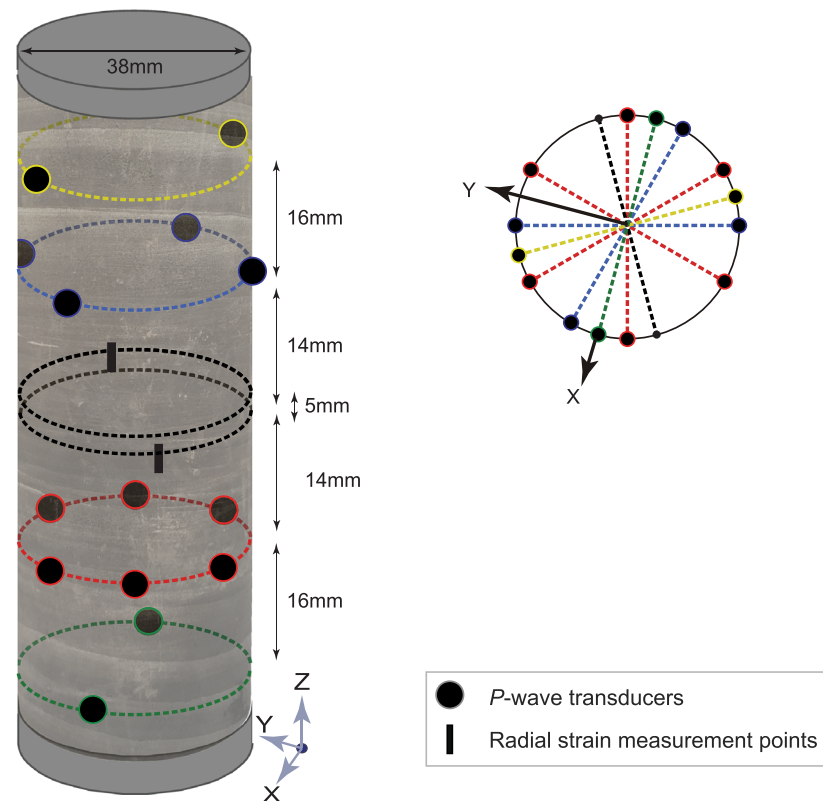


Figure 1. Configuration 14 radially mounted transducers, aligned with the middle of each core sample, after (Douma et al., 2019; Sarout et al., 2015, 2017). Note that this figure is vertically exaggerated for display purposes.

Two aluminum spacers (38 mm diameter; 1 mm thickness) are placed on top and bottom of the partially saturated core plugs (see Figure 1), to achieve macroscopically undrained conditions during the deformation of the rock (i.e., no water in/out at the sample's top, bottom or lateral boundaries). As a result there is no pore pressure control or monitoring possible during testing. The experiments are all performed at room temperature ($22.0 \pm 1.5^\circ\text{C}$). A detailed description of the experimental procedure is given by Douma et al. (2019), summarized as

- An increase in confining pressure at a rate of 0.5 MPa min^{-1} up to 15 MPa, followed by a consolidation stage of about 3 days under isotropic stress conditions, after which all samples reached axial consolidation rates of $\sim 40 \mu\text{m day}^{-1}$.
- Subsequently, an increasing vertical stress was applied along the sample's axis (orthogonal to the bedding) with a constant axial strain rate of $1 \times 10^{-7} \text{ s}^{-1}$ until failure of the WMF sample.

A total of 14 piezoceramic-based *P* wave transducers (effective ultrasonic footprint diameter 6 mm, dominant resonant frequency 0.5 MHz) are directly attached to the sample (see Figure 1), through the Viton sleeve. The transducers are designed and assembled at CSIRO laboratories from a 6 mm compressional Piezoceramic crystal, mounted in a 9 mm aluminum housing in contact with the lateral surface of the sample. Each transducer acts sequentially as a source S_i , while the other 13 transducers act as receivers R_j . During each survey, ten repeat shoot-receive transmissions are performed for each S_i , and the recorded waveforms are stacked at each R_j , thereby improving the signal-to-noise ratio (SNR). Each survey consists of 182 (14×13) stacked waveforms, recorded during a time window of $410 \mu\text{s}$, at a sampling rate of 10 MHz, and an amplitude resolution of 12-bit (Sarout et al., 2015). Surveys are repeated at regular time intervals of either 2.5 or 5 m during a deformation experiment. Each active source survey takes ~ 30 s to complete, in the time between all 14 transducers are switched to passive monitoring mode, allowing the detection and recording of spontaneous fracturing events referred to as AEs. The full waveforms are acquired, with AEs detected by a preset trigger threshold between 10 and 50 mV, depending on the noise level in each channel. In preparation

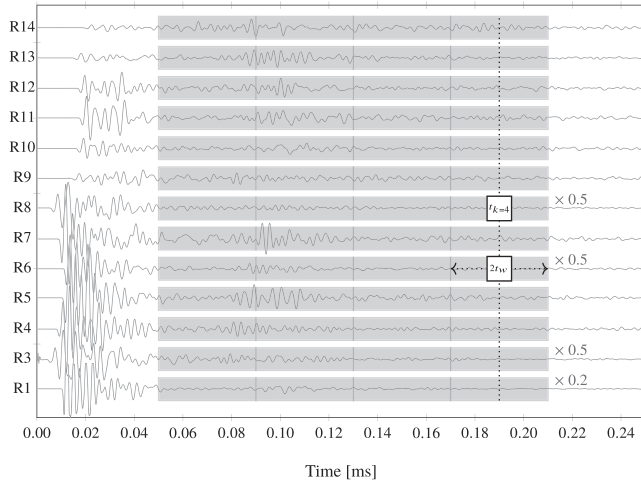


Figure 2. Source 2 shot gather taken from \mathbf{D}_{810} acquired at 105 hr during the monitoring of sample 70% S_w . Waveforms R1, R3, R6, and R8 are scaled for display purposes by the factors indicated. The four nonoverlapping $40 \mu\text{s}/2t_w$ correlation windows beginning at 50 up to 210 μs centered at $t_{k=1}$ to $t_{k=4}$ in coda are indicated by the shaded boxes.

for subsequent processing, the data recorded during each survey p are arranged into an impulse response data cube \mathbf{D}_p (typically around 12 MB in binary format), with each waveform stored corresponding to \mathbf{S}_i in rows, \mathbf{R}_j in columns, for P surveys.

In order to ascertain the actual extent of the fracture network formed during triaxial failure, all tested WMF samples were scanned before and after the triaxial deformation experiment (while jacketed without transducers) using an X-ray computed tomography scanner. The created data set has a voxel size of $100 \times 100 \times 400 \mu\text{m}$.

2.3. CWD Inversion Procedure

This section summarizes the theory and inversion workflow applied to the three impulse response data cubes \mathbf{D}_p obtained from the three triaxial experiments. We apply a linear least squares inversion method, for the time-lapse monitoring of shale deformation and failure under triaxial stress conditions. The version of Python code used during this study is available in Zotz-Wilson (2019). For a detailed description of the theory employed, the reader is referred to Appendix A, which itself is paraphrased from Planès et al. (2015).

The basic premise of CWD is that a change in the scattering properties of a medium (impedance contrast between the medium and scatterers), can be inferred by a comparison between wavefields recorded before and after the change. This comparison is performed via a normalized cross-correlation, with the measured decorrelation coefficient K^m calculated for a time window $[t_k - t_w, t_k + t_w]$ within the coda. Similar to CWI which in its most common application relates the phase shift of this correlation to a change in elastic wavespeed (Grêt et al., 2006b; Larose & Hall, 2009; Payan et al., 2009; Zhang et al., 2012) or temperature (Grêt et al., 2006b; Larose et al., 2006; Weaver & Lobkis, 2000) of the medium, CWD relates the corresponding K^m to a change in the scattering properties of the medium, for a particular time window within the coda. This method rests on the understanding that a window within the early coda wave is sensitivity to a smaller region around the source/receiver than a window in the late coda. By combining this with some knowledge of the evolution of diffusive energy, along with multiple source-receiver pairs, one can formulate an inverse problem to minimize the misfit between the measured K^m and a theoretical estimation K^T of the decorrelation coefficients.

In terms of data processing, for each survey p , the measured decorrelation coefficient K_{ij}^m between a reference survey \mathbf{D}_{ref} and survey \mathbf{D}_p obtained after perturbation, are calculated for each source i and receiver j and nonoverlapping window of width $2t_w$ within the coda. The resulting data decorrelation matrix \mathbf{K}_p^m of dimensions $[\mathbf{S}_i, \mathbf{R}_j, t_k]$ for each survey p , serves as the observed data input to the inversion scheme. The shot gather in Figure 2 illustrates the position of the four nonoverlapping correlation windows used in this study when calculating the K_{ij}^m between survey \mathbf{D}_{ref} and survey \mathbf{D}_p .

In order to relate each K_{ij}^m for various windows within the coda to localized change within the core sample, a theoretical estimation of the decorrelation coefficient K_{ij}^m (Rossetto et al., 2011), associated with a change in scattering at location \mathbf{r} is calculated as

$$K_{ij}^T(\mathbf{r}, t_k) = \frac{V_0 \sigma_T}{2} Q(\mathbf{S}_i, \mathbf{R}_j, \mathbf{r}, t_k), \quad (1)$$

where σ_T is the scattering cross section of a defect at position \mathbf{r} within a medium with a background velocity V_0 . The sensitivity kernel $Q(\dots)$ used in this work was derived by Rossetto et al. (2011) as

$$Q(\mathbf{S}_i, \mathbf{R}_j, \mathbf{r}, t_k) = \frac{1}{4\pi \mathcal{D}} \left(\frac{1}{s_i} + \frac{1}{r_j} \right) \exp \left[\frac{\|\mathbf{S}_i - \mathbf{R}_j\|^2 - (s_i + r_j)^2}{4\mathcal{D}t_k} \right], \quad (2)$$

where $s_i = \|\mathbf{S}_i - \mathbf{r}\|$, and $r_j = \|\mathbf{R}_j - \mathbf{r}\|$ capture the distance between the source/receiver position $\mathbf{S}_i/\mathbf{R}_j$ and the defect at \mathbf{r} . The coefficient \mathcal{D} describes the diffusivity of the wavefield (the rate of diffusive propagation of

energy) within the medium. This kernel quantifies the expected sensitivity of a particular sensor arrangement ($\mathbf{S}_i, \mathbf{R}_j$) at elapse time t_k within the coda to a perturbation at position \mathbf{r} . In other words Equation 2 describes an exponential decay in sensitivity to a change as one moves further away from the source and receiver locations, when making observations at elapse time t_k . This kernel is derived on the assumption of homogeneous diffusive energy propagation (i.e., \mathcal{D} is not spatially dependent) within an infinite medium and therefore does not account for the influence of the core boundary conditions or anisotropic/inhomogeneous materials. While in the works of Planès et al. (2015) and Zhang et al. (2016) the effects of the medium boundaries on the intensity of diffusive energy were accounted for by the method of images (Crank, 1975), here we are faced with sources and receivers located on a cylindrical boundary preventing its application. This study therefore neglects the influence of the core geometry and assumes \mathcal{D} is spatially invariant. For a three-dimensional visualization of sensitivity kernels between different \mathbf{S}_i – \mathbf{R}_j pairs, see Supporting Information S1.

The core volume is then discretized into tetrahedra, allowing Equation 1 to be calculated at the center of each, and the formulation of the forward problem in vector/matrix form as

$$\mathbf{K}_p^m = \mathbf{G}\mathbf{m}, \quad (3)$$

where \mathbf{K}_p^m is arranged into a vector of measured decorrelation coefficients at survey p , for each \mathbf{S}_i – \mathbf{R}_j pair, and correlation window as shown in Figure 2. The matrix \mathbf{G} stores the sensitivity kernels $Q(\mathbf{S}_i, \mathbf{R}_j, \mathbf{r}, t_k)$ row-wise, calculated at each tetrahedron. The true model parameters \mathbf{m} is a vector containing the density of σ_T perturbations within each tetrahedron given as σ_{T_p} with the dimensions mm^2/mm^3 . A region of increased σ_{T_p} therefore indicates a change in the impedance contrast of medium scatterers such as that introduced by fractures.

The least squares formulation described by Tarantola (2005) and Valette and Tarantola (1982) is adopted, in order to invert Equation 3 for estimated model parameters $\tilde{\mathbf{m}}$ which minimize a misfit function with the recorded data (\mathbf{K}_p^m). In other words, the distribution of σ_{T_p} which yield theoretical \mathbf{K}^T close to \mathbf{K}_p^m is determined for time step p . See Appendix A1 for a detailed account of the implementation of the inversion procedure used in this study. It is important to note that for each time step p the inversion procedure does not include any prior information from the previous time step $\tilde{\mathbf{m}}$. This ensures each time step p is independent from one another, and therefore, any observed correlations between successive distributions of σ_{T_p} are derived from the input data \mathbf{K}_p^m . The same four $40 \mu\text{s}$ nonoverlapping correlation windows (beginning at $50 \mu\text{s}$ up to $210 \mu\text{s}$) are used to construct the vector \mathbf{K}_p^m of decorrelation coefficients for each survey p , see Figure 2. The value of $50 \mu\text{s}$ is chosen as the approximate point at which at least a 50% reduction in amplitude for all receivers occurs, after which it is assumed the diffusive transport of energy dominates. The width of each correlation window must be significantly larger than the dominant period T_0 of the wavefield, while the number of windows must be balanced against computational cost.

The wavefield diffusivity \mathcal{D} in Equation 2 is assumed to remain constant throughout each test, and is therefore estimated from a single trace selected at approximately 50% of peak stress by the approach described by Anugonda et al. (2001). The background velocity V_0 is also determined from this single trace based on the P wave arrival, and is held constant throughout the experiment and across each \mathbf{S}_i – \mathbf{R}_j pair. These simplifications are motivated by the observation of previous applications of CWD (Zhang et al., 2018), that the inversion is relatively insensitive to changes in \mathcal{D} , and our own observation that V_0 primarily acts as a scaling parameter to the inversion results.

The core volume is discretized into a tetrahedral mesh of 3.2 mm characteristic length using the Gmsh (Geuzaine & Remacle, 2017), resulting in $\sim 15,000$ cells, thereby keeping the computational time low (~ 5 min on 20 CUPs in parallel). The model parameters $\tilde{\mathbf{m}}$ resulting from each inversion time step p are mapped onto the tetrahedral mesh, providing an indication of the spatiotemporal changes in the density of scattering cross-section σ_{T_p} with respect to the reference data cube \mathbf{D}_{ref} . The reference point is selected toward the beginning of axial stress loading, once confining pressure has been applied, thereby ensuring each ultrasonic transducer is sufficiently coupled to the lateral surface of the WMF sample (see Figure 1). Furthermore, in all cases a comparison is made between the $\tilde{\mathbf{m}}$ distribution resulting from (i) a fixed

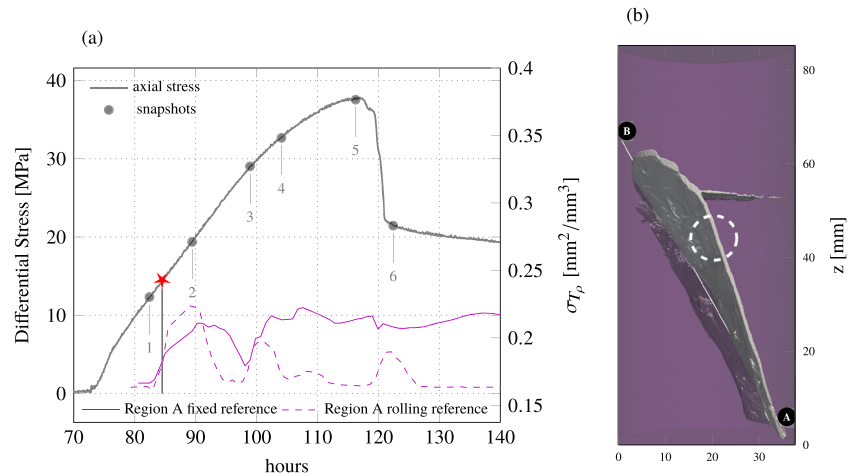


Figure 3. (a) Monitoring of the 70% S_w sample, showing the development in terms of scattering cross-section σ_{T_p} (reference at 80 hr and the rate of change of σ_{T_p} (rolling reference lag of 4.22 hr) for a 4 mm sampling sphere located at the base of the main shear fracture. The annotated \star indicates the identified point at which σ_{T_p} first localizes, while \bullet indicate the snapshots displayed in Figures 4 and 5. (b) X-Ray postdeformation single shear fracture, with a horizontal predeformation dehydration fracture plane at ~ 55 mm. The dashed region was obscured during X-Ray tomography by a transducer and therefore represents an interpretation. See Movie S2 for an isometric view rotation of the fracture network.

reference comparison (i.e., consecutive correlations between \mathbf{D}_{p_i} and \mathbf{D}_{ref}); and (ii) the $\tilde{\mathbf{m}}$ distribution resulting from a rolling reference comparison, (i.e., consecutive correlations between \mathbf{D}_{p_i} and \mathbf{D}_{p_i-N} which lags behind p_i by N surveys). Where large changes in \mathbf{K}_p^m are identified early on during a given deformation experiment, a second \mathbf{D}_{ref} is defined in order to avoid large decorrelation and therefore a reduction in sensitivity to subsequent changes (Zotz-Wilson, Boerrigter, et al., 2019).

3. Results

The analysis of the mudstone samples will be presented from highest to lowest water saturation, that is, 70%, 58%, and 28%. For each sample, the mechanical data including a description of the postfailure macrostructure is discussed, followed by the inversion results in terms of the distribution of σ_{T_p} throughout deformation. In order to quantitatively compare the three-dimensional inversion results with the evolution of stress during axial loading, 4 mm spheres are placed within the center of regions of high σ_{T_p} ; and the average value of all intersected tetrahedra is calculated for each survey/time step throughout the experiment. This allows direct quantitative comparison of the three-dimensional distribution of σ_{T_p} with the changes in differential stress.

The point of initial localization in σ_{T_p} is determined by calculating the Getis and Ord (2010) spatial clustering statistic within a 40 mm sphere where the null hypothesis of no localization is tested with a significance of 0.05 for 999 random samples, and a distance band of 5 mm. For technical details on the implementation of this analysis see the documentation associated with the Python package PySAL (Rey & Anselin, 2007). In all cases, rolling reference monitoring is performed to ensure the rate-of-change in σ_{T_p} correlates with the fixed reference results, thereby avoiding a spurious correlation after sudden large or prolonged changes in the medium (Zotz-Wilson, Boerrigter, et al., 2019). For the samples of lower initial water saturation (58% and 28%), two fixed reference points before and after large changes in σ_{T_p} are defined. For the 70% S_w sample, in which only a single large shear fracture formed (Figure 3b), only a single reference point is necessary. For each deformation experiment we report the evolution of differential stress with time, including the 3 days of consolidation under isotropic stress preceding the axial loading stage.

No AEs were detected during the (1.8 or 4.5 min) period of passive monitoring between each consecutive active survey. Therefore, for the applied strain rate of $1 \times 10^{-7} \text{ s}^{-1}$, and saturation levels, the Whitby Mudstone did not produce AEs of sufficient magnitude to be detectable.

3.1. Sample With 70% Initial Water Saturation

For the 70% S_w sample shown in Figure 3a, the onset of nonlinear deformation occurs at ~ 294 MPa, toward a maximum differential stress of 37.8 MPa at 117 hr. This is followed by a two-stage reduction initially toward 36.2 MPa at 119 hr, and then a larger reduction toward 22.8 MPa at 121 hr. For the remainder of the test a stage of gradual reduction in differential stress occurs. The postmortem X-ray CT image of the sample shown in Figure 3b reveals a single large shear fracture extending from the base of the core (Point A) up until ~ 60 mm as indicated by Point B. The single bedding parallel fracture at ~ 55 mm is present in both the predeformation and postdeformation X-ray CT scans. See Movie S2 for an isometric view rotation of the fracture network.

The changes in the distribution of σ_{T_p} in the region of Point A, relative to the fixed reference show an initial increase at 14.5 MPa or 38% of the peak stress, see solid curve in Figure 3a. This initial increase peaks at 90 hr, for a differential stress of ~ 20 MPa, before reducing again and reaching a local minimum of ~ 26 MPa at 98 hr. This is immediately followed by a second sharp increase, around the onset of nonlinear deformation. A third smaller rise occurs at ~ 106 hr, followed by a smaller reduction up until ~ 113 hr. A final slight increase in σ_{T_p} leading up to peak stress at 37.8 MPa occurs, followed by a slight drop coinciding with the point of failure. This is followed by ~ 20 hr of gradual increase in σ_{T_p} , plateauing out toward the end of the experiment.

The rolling-reference dashed curve in Region A (Figure 3a) provides an indication of the rate-of-change in σ_{T_p} over a 4.22 hr period. This curve shows its largest value at 89 hr followed by peaks of reducing magnitude coinciding with the increase noted in the fixed-reference results at 102 and 108 hr. This provides confidence in the fixed-reference distribution of σ_{T_p} . At the peak stress, a final larger increase in the rolling reference σ_{T_p} curve occurs.

The six snapshots taken at the times denoted by the plain disks \bullet shown in Figure 3a, display the σ_{T_p} distribution for both x - z slices (Figure 4), and slices parallel to the A-B postdeformation fracture plane (Figure 5). See these figures covering the entire experiment in Movie S5. The differences between the first two time steps ($\bullet_1 - \bullet_2$) in both figures show a localized increase in σ_{T_p} toward Point A, with some distribution along the plane A-B. As stress increases, the point of largest σ_{T_p} moves further downward along plane A-B, with a region around Point B also showing increased σ_{T_p} , slightly skewed to the right side of plane A-B, see Point B in Figure 5. Further, there is a reduction in the distribution around Point B and an increase in the extent at Point A before ($\bullet_4 - \bullet_5$) and after ($\bullet_5 - \bullet_6$) failure. The x - z slices (Figure 4) also capture the downward movement and increase in σ_{T_p} toward Point A.

3.2. Sample With 58% Initial Water Saturation

The 58% S_w sample test shown in Figure 6a exhibits the onset of nonlinear deformation at ~ 36 MPa/ ~ 100 hr, with a maximum differential stress of 51.3 MPa at 131 hr. This is followed by three stages of reduction toward 44.2 MPa at 139.5 hr, and then a larger sudden drop to 27 MPa at 140 hr. For the remainder of the test a continuous gradual reduction in differential stress occurs. The postmortem X-ray CT image of the sample shown in Figure 6b reveals a large shear fracture extending from the lower right (A) of the x - z slice, up until ~ 58 mm on the left (B). A second shear fracture is also evident extending from the approximate center of the x - z slice (Point C) up until Point D at ~ 37 mm. The region of this smaller fracture around Point C appears to show greater compliance (more closed) than the region around Point D. The single bedding parallel fracture at ~ 43 mm is present in both the predeformation and postdeformation X-ray CT scans. See Movie S2 for an isometric view rotation of the fracture network.

The CWD inversion results indicate an initial increase in σ_{T_p} coinciding with Region D, peaking at ~ 100 hr/ ~ 35 MPa, see Figure 6a. The distribution of this initial increase is captured at the \blacktriangle snapshots, shown in Figure 7 or in Movie S6. Between $\blacktriangle_1 - \blacktriangle_3$ upward drift in the location of maximum σ_{T_p} occurs, followed by an increase in both magnitude and spatial distribution from $\blacktriangle_4 - \blacktriangle_5$. The final snapshot (\blacktriangle_6) shows the subsequent reduction in magnitude and spatial distribution. At 98 hr just prior to the peak σ_{T_p} in Region D, an increase occurs in Regions A and B (see respective curves in Figure 6a). The six \blacksquare snapshots shown in Figure 8 indicate a progressive increase in σ_{T_p} toward Point B, continuing all the way to peak stress at 51.3 MPa. The x - z sliced distribution reflecting the \bullet snapshots generated from a reference at 90 hr

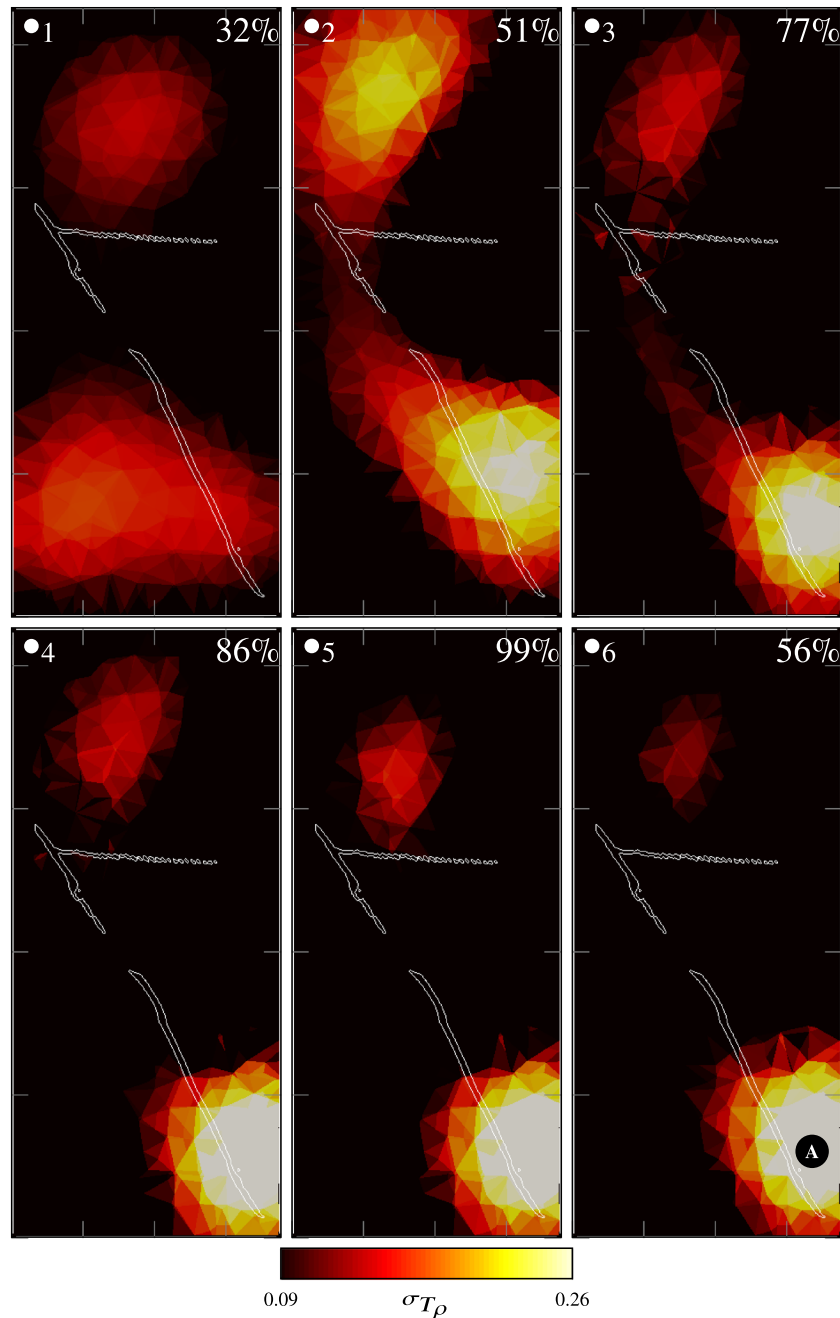


Figure 4. The 70% S_w sample sliced along the x - z plane for time steps •₁ to •₆ as indicated by the • symbols in Figure 3a. The corresponding percentage of peak stress is indicated in the upper right corner of each slice. Point A indicates the position of the 4 mm sampling sphere at •₆. The distribution of σ_{T_p} initially localizes at •₂ and then drifts downward, displaying increased focus in Region A, prior to (•₅), and after (•₆), failure. See this figure in Movie S5.

(Figure 9) show a process by which the region of largest σ_{T_p} alternates between Regions D and A (•₁–•₄), and then focuses at A just prior (•₅) to, and after (•₆) the point of dynamic failure. See both the x - z and major fracture slice in Movie S7.

3.3. Sample With 28% Initial Water Saturation

The 28% S_w sample test shown in Figure 10a exhibits the onset of nonlinear deformation at ~ 58 MPa/ ~ 126 hr, with a maximum differential stress of 87.0 MPa at 164 hr. This is followed by a reduction toward 34.8 MPa at

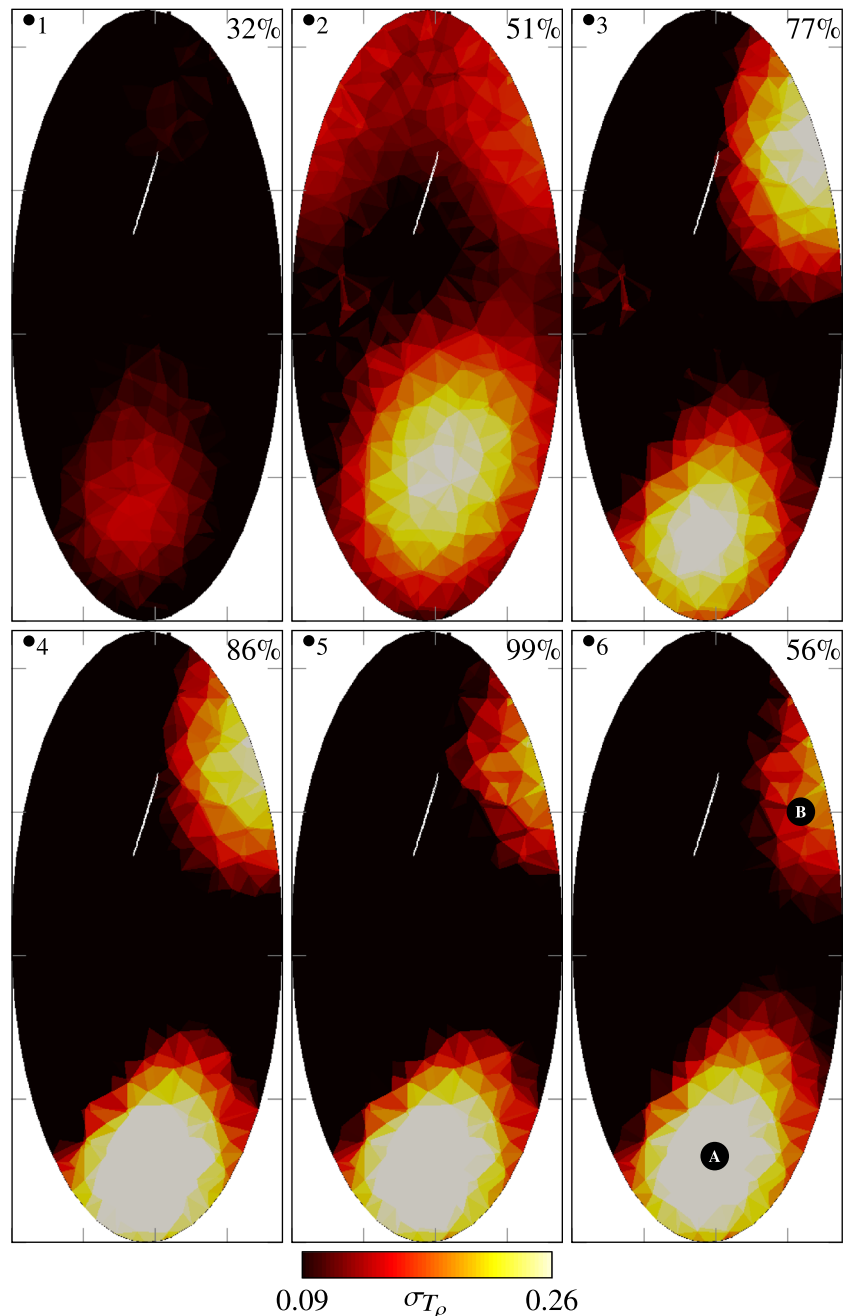


Figure 5. The 70% S_w sliced parallel to the fracture plane A-B, for time steps •₁ to •₆ as indicated by the • symbols in Figure 3a. The corresponding percentage of peak stress is indicated in the upper right corner of each slice. Point A indicates the position of the 4 mm sampling sphere at t_6 , while Point B shows the position of the maximum σ_{T_p} around the fracture tip. The distribution of σ_{T_p} initially localizes at •₂ and then drifts downward, displaying increased focus in Region A, prior to (•₅), and after (•₆), failure. See this figure in Movie S5.

168 hr, and then an increase to 39.4 MPa at 169 hr. For the remainder of the test a continuous gradual reduction in differential stress occurs. The postmortem X-ray CT image of the sample shown in Figure 10b consists of one large shear fracture, traversing from the lower left to upper right of the x - z slice (A-B), with preexisting genetic dehydration fracture planes at the bottom (E) and two at the top (F) of the core. Around the base of the large fracture (A), several smaller fractures coalesce into a single fracture (C-D). Careful

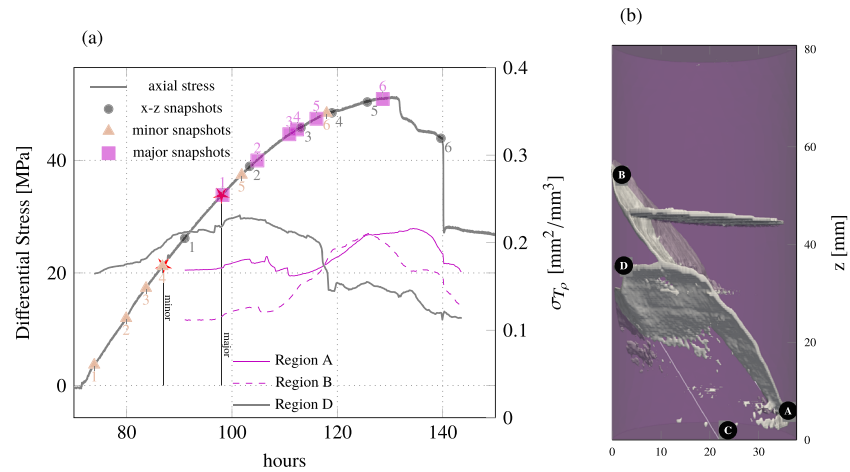


Figure 6. (a) Monitoring of the 58% S_w sample, showing the fixed-reference development in terms of scattering cross-section σ_{T_p} for three 4 mm spheres located within the minor and main shear fractures. The annotated \star indicates the identified point at which σ_{T_p} first localizes, while \bullet , \blacktriangle , and \blacksquare indicate the snapshots displayed in Figures 7–9. (b) X-Ray postdeformation major (A-B) and minor (C-D) shear fractures, with a preexisting dehydration fracture plane at ~ 45 mm. See Movie S3 for an isometric view rotation of the fracture network.

inspection of the postdeformation X-Ray scans indicates several smaller fractures, most of which are on one side of the main shear fracture, though there also exists a smaller fracture which originates from two conical low-density heterogeneities (E) at the base of the core. Furthermore, the dashed region in Figure 10b from the base of the core up until the lower dehydration fracture at E, was damaged during testing and subsequently this region fell off when the core was extracted from the pressure vessel. For the first ~ 10 min of

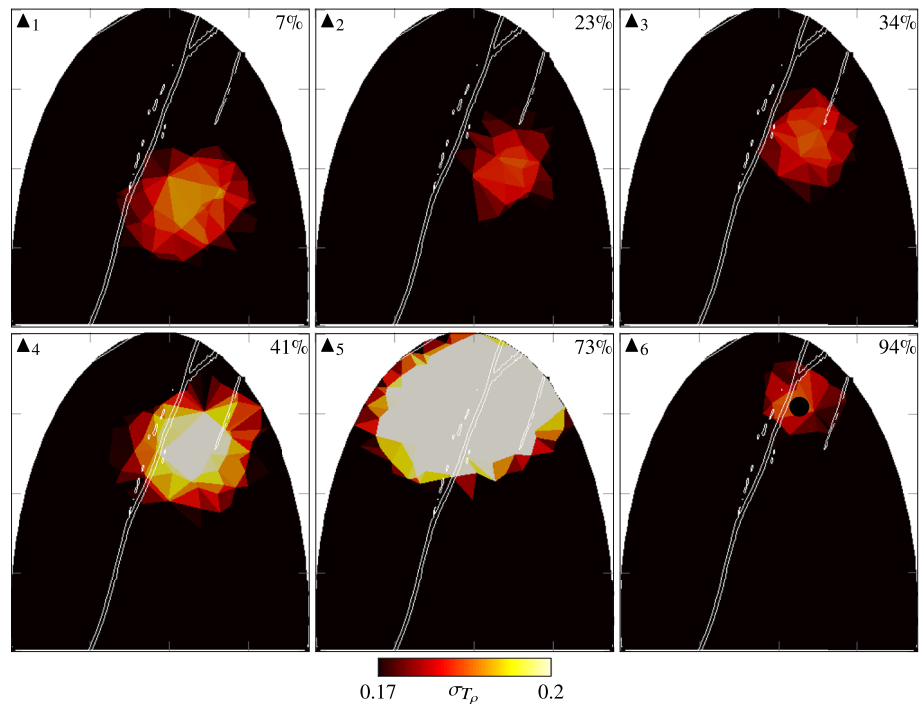


Figure 7. The 58% S_w sample sliced along the minor fracture plane C-D, for time steps \blacktriangle_1 to \blacktriangle_6 as indicated by the \blacktriangle symbols in Figure 6a. The corresponding percentage of peak stress is indicated in the upper right corner of each slice. Point D indicates the position of the 4 mm sampling sphere at t_6 . The focal point of the distribution of σ_{T_p} moves upward between \blacktriangle_1 and \blacktriangle_3 and then increases in magnitude and spatial extent between \blacktriangle_4 and \blacktriangle_5 . Subsequent reduction in the magnitude of σ_{T_p} occurs toward \blacktriangle_6 . See this figure in Movie S6.

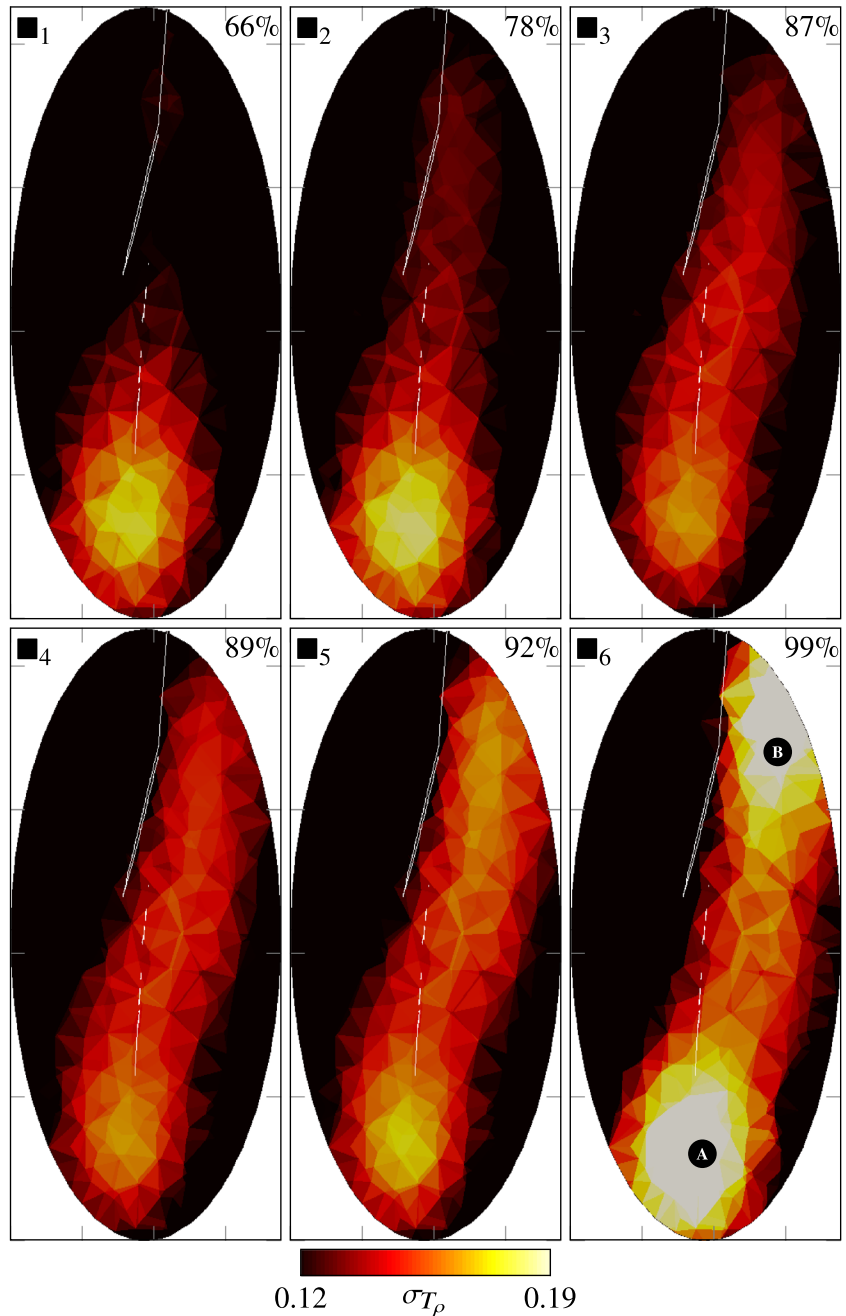


Figure 8. The 58% S_w sample sliced along the fracture plane A-B, for time steps \blacksquare_1 to \blacksquare_6 as indicated by the \blacksquare symbols in Figure 6a. The corresponding percentage of peak stress is indicated in the upper right corner of each slice. Points A and B indicate the position of the 4 mm sampling sphere at t_6 . The distribution of σ_{T_p} increases from Point A toward Point B between \blacksquare_1 and \blacksquare_6 . A notable increase in its magnitude at both A and B occurs at \blacksquare_6 . See this figure in Movie S7.

experimentation the applied strain rate is $1 \times 10^{-6} \text{ s}^{-1}$ up until 7 MPa of axial stress, after which it is reduced to $1 \times 10^{-7} \text{ s}^{-1}$ for the remainder of the test. See Movie S4 for an isometric view rotation of the fracture network.

During this period of increased strain rate, in the center Region C-D, an increase in σ_{T_p} occurs, the spatial distribution of which is captured by the \blacksquare snapshots indicated in Figure 10a and displayed in Figure 11. See both figures in Movie S8. While the first two time steps $\blacksquare_1 - \blacksquare_2$ show almost the same distribution, the third \blacksquare_3 indicates an increase in magnitude and upward movement. This is then followed ($\blacksquare_4 - \blacksquare_6$)

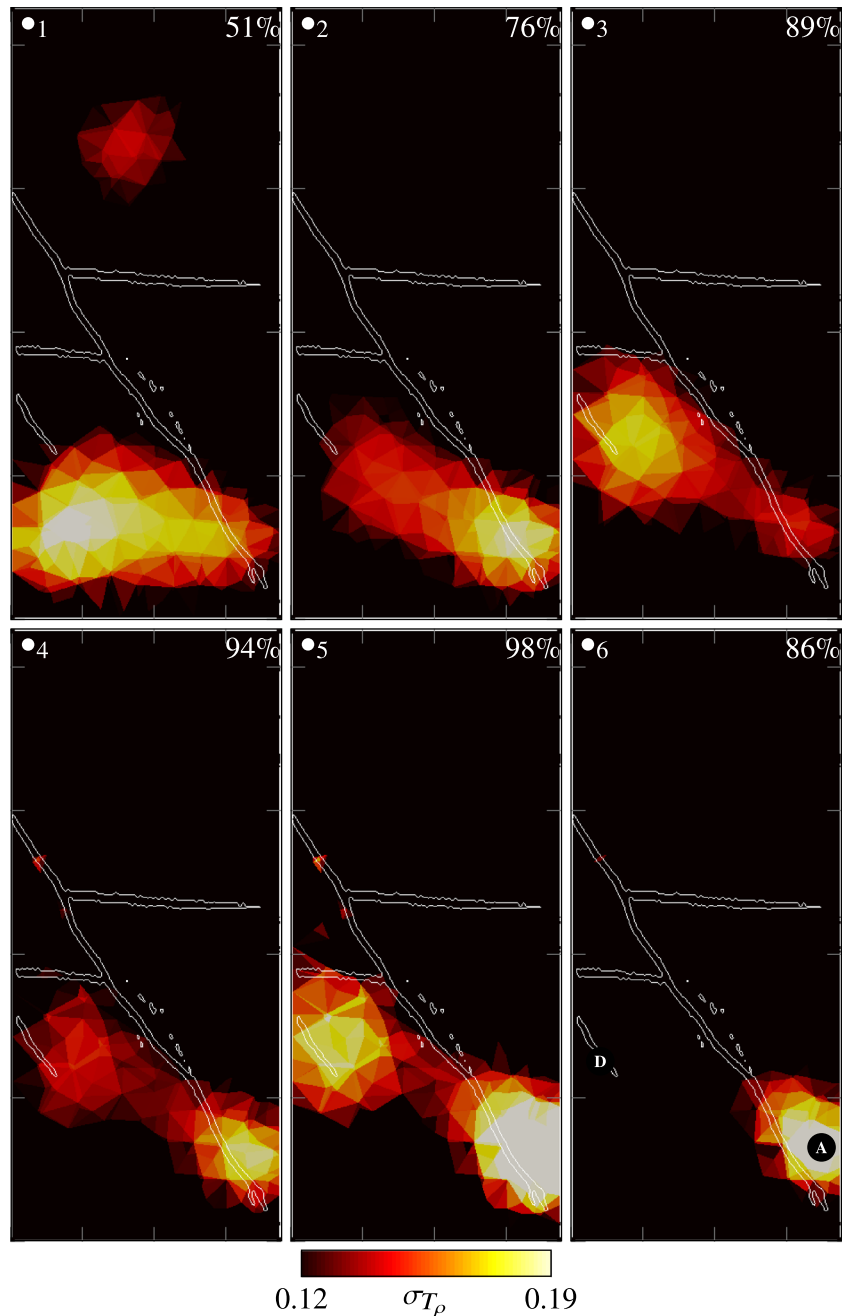


Figure 9. The 58% S_w sample sliced along the x - z plane for time steps \bullet_1 to \bullet_6 as indicated by the \bullet symbols in Figure 6a, and a reference at 90 hr. The corresponding percentage of peak stress is indicated in the upper right corner of each slice. Points A and D indicate the position of the 4 mm sampling spheres at t_6 . The distribution of σ_{T_p} alternates between Regions D and A twice (\bullet_1 to \bullet_4). At \bullet_5 prior to failure, Region A shows greater σ_{T_p} than Region D. After failure at \bullet_6 only Region A displays a focused region of σ_{T_p} . See this figure in Movie S7.

by an increase in the spatial distribution and magnitude of σ_{T_p} . Shortly afterward a subsequent reduction in σ_{T_p} occurs. In order to improve sensitivity to subsequent changes, a reference point is defined at 105 hr. The results from this redefined reference show an increase in σ_{T_p} within Region E, and around F. See the \bullet snapshots indicated in Figure 10 and displayed in Figure 12. See both figures in Movie S9. This center of maximum σ_{T_p} around E moves downward as it increases (\bullet_1 – \bullet_3), up until 130 hr, at which point a gradual reduction begins. During \bullet_1 – \bullet_3 we also note a region of increasing σ_{T_p} around F. After peak

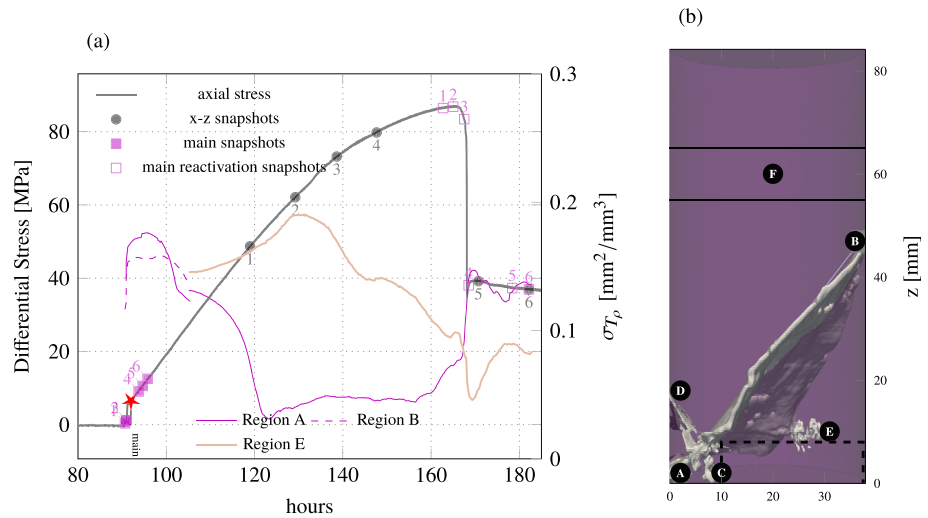


Figure 10. (a) Monitoring of the 28% S_w sample, showing the fixed-reference development of σ_{T_p} at the base and tip of the main fracture, and in a region surrounding the high-density impurities. Note the dashed, Region B curve is only shown for the fixed-reference distribution at the beginning of the stress increase. The annotated \star indicates the identified point at which σ_{T_p} first localizes, while \bullet , \blacksquare , and \square indicate the snapshots displayed in Figures 11–13. (b) X-Ray postdeformation major (A-B) and minor (C-D) shear fractures, with preexisting dehydration fracture planes above and below F and below E. Two low-density impurities present in the sample are indicated at Point E. The dashed regions below E was damaged during testing and therefore was not present during X-Ray tomography. See Movie S4 for an isometric view rotation of the fracture network.

stress is reached at ~ 167 hr a rapid redistribution of σ_{T_p} over the plane A-B occurs (Region A curve in Figure 10a), which increases postfailure, between \bullet_5 and \bullet_6 . This reactivation of the region surrounding plane A-B is spatially captured by the \square snapshots shown in Figure 13 and in Movie S9, which shows minimal increase between \square_1 and \square_2 prior to peak stress, followed by increased distribution $\square_3 - \square_6$ after failure.

3.4. Comparative Analysis

For each of the samples of varying initial S_w , an initial increase in σ_{T_p} is determined, based on the Getis and Ord (Getis & Ord, 2010) spatial clustering statistic. This point is marked in Figures 3, 6, and 10 by a \star . For the 70% and 58% S_w samples an increase in localized σ_{T_p} is found at 14.5 and 21.3 MPa, respectively, while for the 28% S_w this occurs at 6.5 MPa, see Figure 14. Additionally, we identify a negative correlation between S_w and the peak differential stress achieved during each test (Douma et al., 2019).

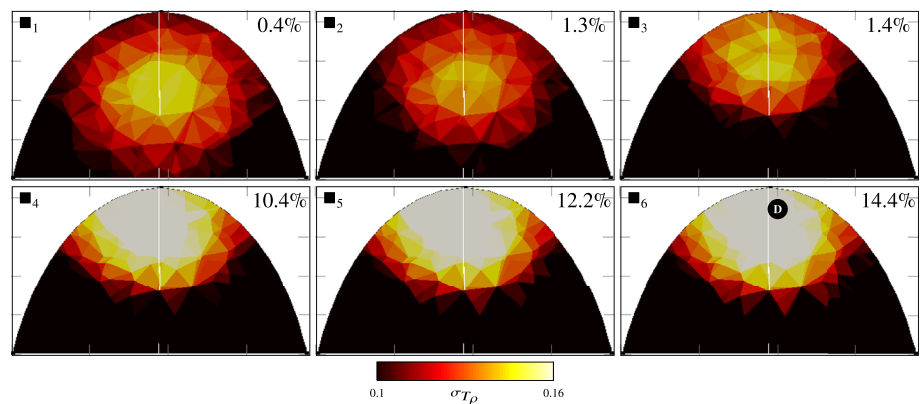


Figure 11. The 28% S_w sample sliced along the minor fracture plane C-D, for time steps \blacksquare_1 to \blacksquare_6 as indicated by the \blacksquare symbols in Figure 10a. The corresponding percentage of peak stress is indicated in the upper right corner of each slice. Point D indicates the position of the 4 mm sampling sphere at t_6 . The focal point of the distribution of σ_{T_p} moves upward between \blacksquare_1 and \blacksquare_5 and then increases in magnitude between \blacksquare_4 and \blacksquare_6 . See this figure in Movie S8.

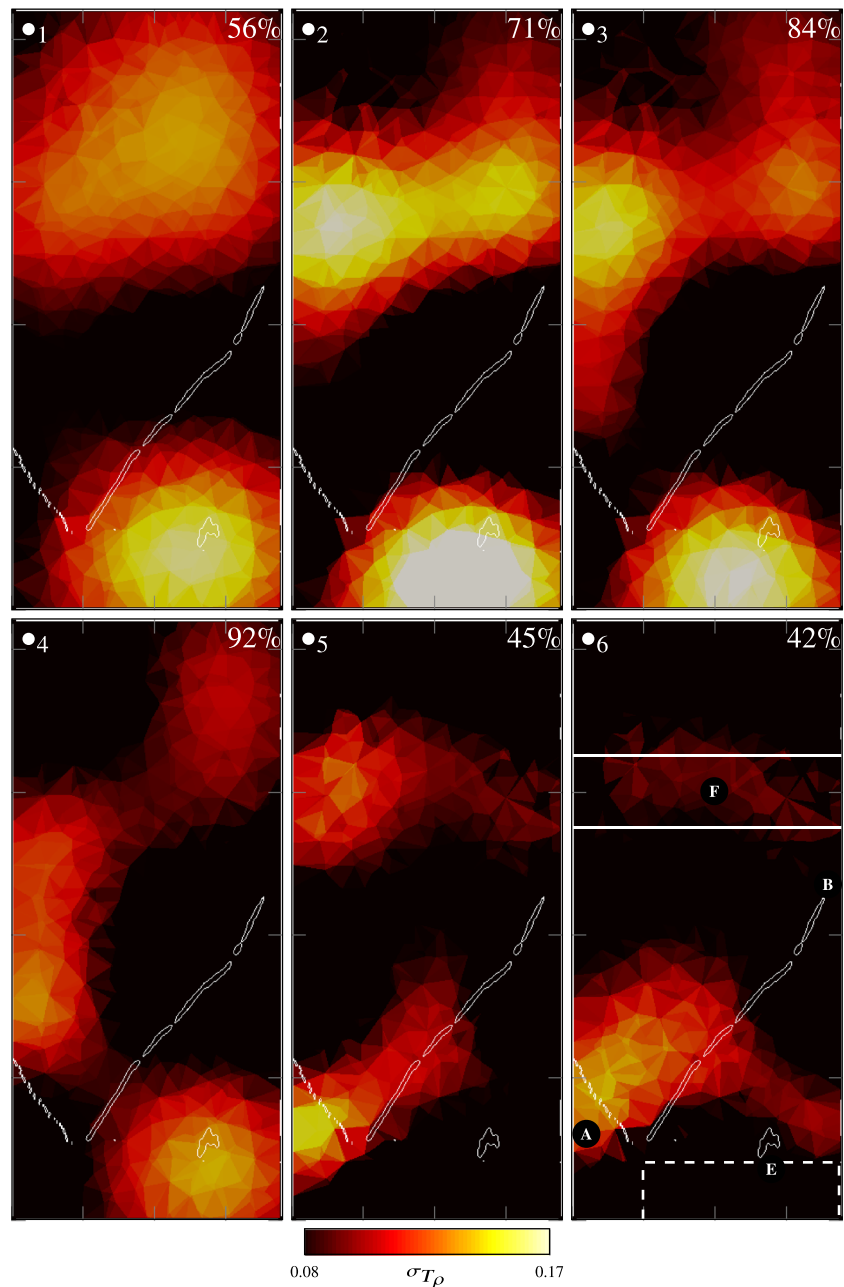


Figure 12. The 28% S_w sample sliced along the x - z plane for time steps \bullet_1 to \bullet_6 as indicated by the \bullet symbols in Figure 10a. The corresponding percentage of peak stress is indicated in the upper right corner of each slice. Points A and E indicate the position of the 4 mm sampling spheres at t_6 . Point F indicates the dehydration planes; Point E the low-density inhomogeneities; and B the main fracture tip. Between \bullet_1 and \bullet_3 the $\sigma_{T\rho}$ distribution increases in magnitude and focus around Regions E and F. At \bullet_4 a reduction in both regions magnitude and distribution occurs. The postfailure snapshots (\bullet_5 to \bullet_6) show distribution from Region A toward Region B and within Region F. See this figure in Movie S9.

The relationship between the differential stress normalized by each sample peak stress with volumetric strain is shown in Figure 15. All core samples show an initially positive compactive response though become dilatative prior to failure. Here both the 70% and 58% S_w samples show the identified initial focus in $\sigma_{T\rho}$ (\star) to occur within the compactive region, prior to the onset of dilatancy.

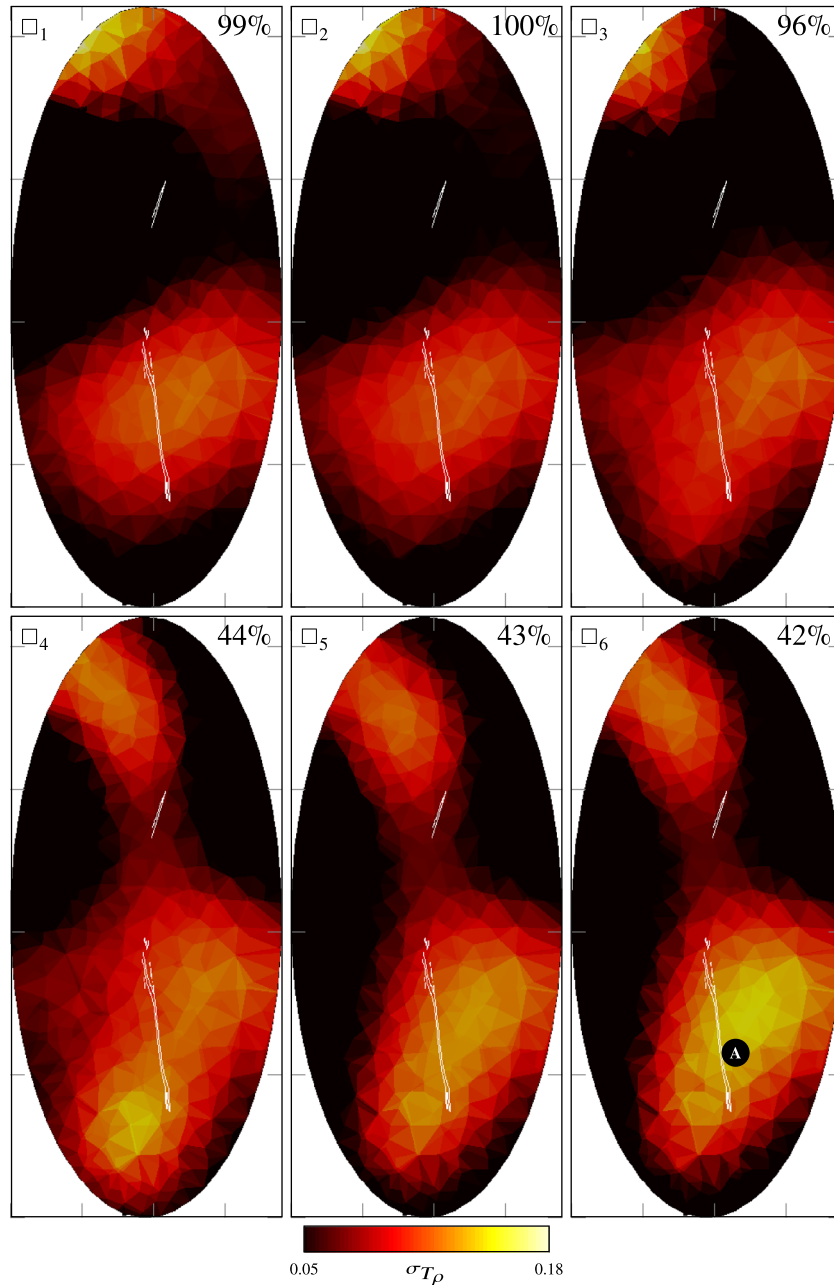


Figure 13. The 28% S_w sample sliced along the main fracture plane A-B, for time steps \square_1 to \square_6 as indicated by the \square symbols in Figure 10a. The corresponding percentage of peak stress is indicated in the upper right corner of each slice. Point A indicates the position of the 4 mm sampling sphere at t_6 . Between \square_1 and \square_3 there is a slight increase in the σ_{T_p} distribution in Region A, while between \square_3 and \square_4 a rapid increase occurs across the plain A-B. From \square_4 and \square_6 the magnitude σ_{T_p} increases in Region A. See this figure in Movie S9.

4. Discussion

4.1. The Development of the Fracture Network as Interpreted From the Distribution of Scattering Cross Section

The application of CWD inversion in monitoring the triaxial deformation of three mudstones of varying initial water saturation, indicates progressive and repeated redistribution of inelastic strain within the rock following strain localization events. Here we define microscopic inelastic strain as associated with inelastic closure, opening or shearing along microscopic fractures, while macroscopic inelastic strain refers to the

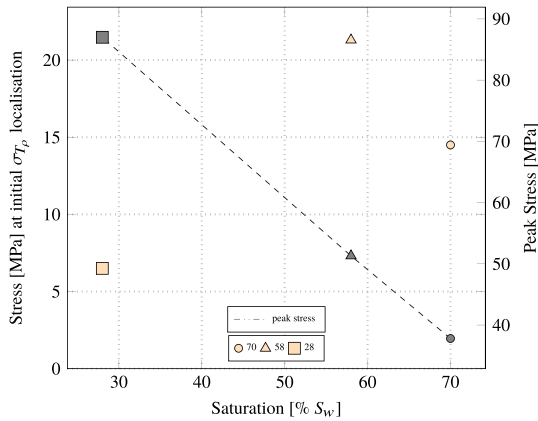


Figure 14. Comparison between the interpreted onset of localized inelastic strain on the left axis and differential peak stress on the right axis, versus initial water saturation of each core sample.

coalescence of microscopic cracks into a large shear fracture. While the method of CWD is in principle also sensitive to elastic closure, opening and shearing of preexisting fractures, we assume that the majority of the crack space is closed after the 3 days of consolidation prior to loading. This assumption is supported by firstly, the predeformation X-ray tomography scans of each sample which show no cross-bedding fractures and secondly, Douma et al. (2019) which indicates that for WMF samples from the same series, the velocity increases and then stabilize during the 3 day consolidation period at a hydrostatic pressure 25 MPa. A region of increased σ_{T_p} can therefore be interpreted as initial localized microscopic inelastic strain and eventually the formation of macroscopic fractures. An increase in spatial distribution indicates the growth of a cracked region, while the increase in magnitude of σ_{T_p} indicates either an increase in the crack density and/or an increase in the impedance contrast between the cracks and the rock matrix, which can be interpreted as a change in the aperture of the cracks/fractures. While the initial localization in σ_{T_p} is interpreted as associated with inelastic strain, a portion of elastic opening/shearing along any preexisting fractures not visible in the predeformation X-ray tomography scans is possible.

For the most saturated sample, there are three stages of increase, followed by a decrease in σ_{T_p} within the region of the base of the main shear fracture (Point A in Figure 3b). This suggests initial localized strain occurs in the form of microscopic fractures, which is subsequently closed as the associated stress is reduced and redistributed throughout the rest of the sample. The reactivation of the same region and the increase in both the distribution (spatial extent) and magnitude of σ_{T_p} suggests an increase occurs in the width, and aperture of the fractures, respectively. This is evident when viewing the slice along the fracture plane (Figure 5 or Movie S5), where only after reactivation at 98 hr (\bullet_3) does the spatial distribution of σ_{T_p} notably increase at both the base (A) and tip (B) of the fracture. This coincides with the onset of nonlinear inelastic deformation or the yield point of the sample. The subsequent reduction in σ_{T_p} distribution at the tip (B) and increase at the base (A) before (\bullet_4 – \bullet_5), and after (\bullet_5 – \bullet_6) failure, indicates that the fracture plane grows laterally at the base while the tip closes up. Further, the observed reduction in the maximum rate-of-change in σ_{T_p} over the first three activations in the region of the fracture base (dashed curve in Figure 3a) suggests a linear reduction in the rate at which the micro/macroscopic fractures open.

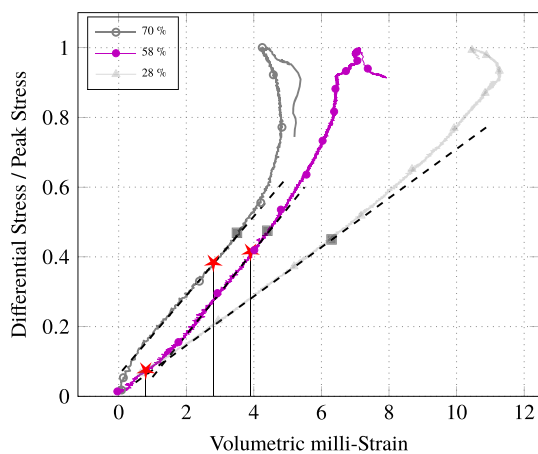


Figure 15. The differential stress, normalized by each samples peak stress, is compared with the volumetric millistrain. The point of identified initial localization in σ_{T_p} is indicated by \star , which for the 70% and 58% samples occurs within a region of approximately linear change, prior to the onset of dilatancy which is identified by the \blacksquare symbols.

The distribution of σ_{T_p} during the 58% S_w test also displays a process of continuous redistribution of stress, though in this case between a region corresponding to the postmortem minor (C-D) and major (A-B) fractures in Figure 6b. Initially, in a region surrounding the postmortem minor fracture (C-D) at ~ 82 hr, we interpret the formation of microscopic inelastic strain. Growth occurs in both magnitude and distribution at ~ 89 hr (see \blacktriangle_4 in Figure 7 or Movie S6), indicating larger scale coalescence occurs at this point. At 98 hr, the main fracture appears to initiate, from the base (A) which again corresponds to the classically determined yield point of the sample. With continued deformation the σ_{T_p} distribution moves toward the tip (B), and eventually fails the sample. Throughout the test we identify approximately four stages of redistribution in σ_{T_p} (see \bullet_1 – \bullet_4 in Figure 9 or Movie S7) between the minor and major fracture. This is interpreted as several stages of opening and closure of initially microscopic and eventually macroscopic fractures, as stress redistribution occurs.

The sample with the lowest initial water content (28% S_w) with its postmortem major (A-B in Figure 10b), and minor (C-D) fractures, show a similar process of redistribution of σ_{T_p} . However, a notable difference with this sample is the presence of the two predeformation low-density,

approximately conical heterogeneities (Region E in Figure 10b) at the lower end of the core. These are interpreted as the void left by leached exoskeleton (fossils) of gastropods such as the *Neptunea contraria* (Linnaeus, 1771). The distribution of σ_{T_p} supports an interpretation where initially the minor fracture (C-D) experiences localized strain at the base of the core, during the initial region of increased strain rate, see snapshots ■ in (Figure 11) or Movie S8. This is followed by gradual prolonged fracturing of a large region surrounding the low-density impurities, see •₁–•₄ in Figure 12 or Movie S9. Subsequently the major shear fracture (A-B) develops (□₄–□₆ in Figure 13 and •₅–•₆ in Figure 12 or Movie S9) close to peak stress, and the failure of the sample. This interpretation is supported by the fact that the region surrounding the interpreted marine exoskeletons (E) was fractured to the point that it fell off the end of the sample once removed from the pressure vessel. Additionally, the concentration in σ_{T_p} between the two preexisting dehydration fractures (F), particularly between •₂–•₃ in Figure 12, indicates that either a change in compliance occurs over these interfaces, or microscopic changes occur within the region between them (a layer of different mineralogy or microstructure).

In summary, for all tested samples the identified localization in σ_{T_p} was found early on during deformation, between 7% and 38% of the peak differential stress and prior the onset of dilatancy (see Figure 15). We therefore interpret this initial localization in σ_{T_p} for the two higher S_w samples, not as the formation of macroscopic coalesced shear fractures but primarily driven by distributed intergranular opening, closure, and shearing at the microscopic scale. The presence of localized impurities in the 28% S_w sample likely resulted in earlier macroscopic damage as was evident postexperimentation. A similar conclusion was reached in a recent study by McBeck et al. (2018) on the Green River shale, during which core samples were time-lapse imaged by X-Ray microtomography while under confining pressure. The identification of localized strain regions became apparent at 35% of the peak differential stress, preceding macroscopic shear failure. This value is consistent with the upper limit of the range reported here. The interpretation of microscopic fracture formation within the inelastic region (before dilatancy) for WMF is supported by Douma et al. (2019) on samples from the same block as the current study, where inelastic wave-speed changes were observed, conducive with microfracturing. Further, McBeck et al. (2018) demonstrate that microscopic opening, closure, and shearing work together to eventually produce macroscopic shear failure. Their observations support our interpretation of a complex timeline of locally increasing (opening or shearing) and decreasing (closure of micro/macroscopic fracturing) σ_{T_p} up until failure.

It is also interesting to note that the observed initial distribution of σ_{T_p} in the x - z snapshots shows similar contours to the expected regions of stress concentration for a cylindrical core (2:1 length to diameter ratio) as described by Paterson and Wong (2005). While this is most evident at the beginning of Movies S5 and S8, it is also shown by the •₁ snapshot in Figure 4. This observation while intriguing, should be interpreted with caution as it may be strongly influenced by the arrangement of receivers. Further investigation with more dense receiver spacing should help to better assess the nature of this observation.

4.2. The Impact of Water Saturation

The Whitby Mudstone plugs display an increase in strength and a reduction in plasticity with a reduction in water saturation (Douma et al., 2019). The primary mechanism driving these changes is expected to be an increase in the capillary suction within the pore space of the mudstone (Ferrari et al., 2014; Fjær et al., 2008; Ramos da Silva et al., 2008). As the pore fluid evaporates from the mudstone, a reduction in the pore-pressure occurs, leading to a tensile stress or negative pressure, and finally a change in compliance (or stiffness) between individual grains (Ewy, 2014; Forsans & Schmitt, 1994; Onaisi et al., 1994). This ultimately leads to an increase in the strength and a reduction in the plasticity of the material. Our experimental results corroborate this relationship which has been recently confirmed for the Whitby Mudstone (Douma et al., 2019) as well as other mudstones (Ghorbani et al., 2009; Ramos da Silva et al., 2008; Vales et al., 2004). The pore pressure distribution within the samples is likely not equal, due to differences in layering (Douma et al., 2019) and therefore permeabilities. Further, while it is not possible to measure the evolution of pore-pressure distribution, or for partially saturated samples, the bulk response at the sample ends, it is expected that a gradual increase in pore-pressure occurs with deformation. Such changes in pore pressure are expected to influence the mechanical behavior, as effective stress is an important estimator of peak stress. The failure of the partially saturated Whitby Mudstone occurs in the brittle domain,

where shear failure results in the formation of dilative fracture planes (Douma et al., 2019). Furthermore, the comparison between the identified onset of inelastic strain (microscopic damage), and initial water saturation suggests a nonlinear relationship, see Figure 14. However, this may be also due to the added inhomogeneity of the low S_w sample (the low-density heterogeneity), or the higher initial strain rate, and therefore more measurement points are required to statistically validate this argument.

As no AEs were detected during passive monitoring of the samples, this suggests that the brittle failure necessary to generate AEs is insufficient (Main, 1990) to overcome the environmental noise.

4.3. CWD: An Effective Real-Time Fracture Monitoring Tool

This study on samples from the WMF indicates that CWD inversion has the potential to image the initiation, propagation and branching of fractures or other heterogeneities, tested under realistic subsurface conditions (stress, pressure, temperature). While there are several other techniques which provide spatiotemporal information on inelastic strain at in situ conditions, they often require substantial investment in equipment and postprocessing, or are inherently less sensitive to subtle localized microscopic changes.

Time-lapse synchrotron microtomography undoubtedly provides the highest spatial resolution, as it is able to resolve the detailed structure of macroscopic fractures (Kandula et al., 2018; Renard et al., 2017, 2018), and microscopic strain localization through digital volume correlations (Mao & Chiang, 2016; Mao et al., 2019; McBeck et al., 2018). The main limitation of this method is that it requires access to an X-ray beam in a synchrotron of sufficient energy to image a sample housed within a bespoke pressure vessel. Further, the maximum sample size is strictly constrained by both the spatial and temporal resolution requirements, while the maximum stress magnitudes are typically less than those achievable within traditional test apparatus.

Traditional acoustic imaging methods such as velocity tomography, while more affordable, and able to provide sufficient spatiotemporal resolution to resolve the region around macroscopic fractures (Aben et al., 2019; Brantut, 2018; Jansen et al., 1993), have not shown sensitivity to microscopic inelastic strain localization, which are often below the optical resolution limit of the probing wavefield.

Passive AEs monitoring is a well established technique in experimental rock mechanics, and with a sufficiently accurate velocity model is able to provide a spatiotemporal indication of the occurrence of brittle failure (Aben et al., 2019; Brantut, 2018; Jansen et al., 1993; Lei et al., 2004; Sarout et al., 2017). However, as demonstrated by this study on the WMF, AEs monitoring relies on the existence of seismicity of sufficient magnitude and frequency to be detected by the available sensor network. For clay- or calcite-rich rocks, where inelastic deformation can develop in a plastic, relatively silent fashion (Peng & Yang, 2018), AEs monitoring is a less suitable method to determine the onset of inelastic strain.

In summary, CWD inversion monitoring requires little to no additional investment in equipment where acoustic monitoring is already available. Further, it is more sensitive to subtle changes in scattering or velocity than methods which rely on the coherent arrivals (Zotz-Wilson, Boerrigter, et al., 2019), and once appropriate inversion parameters are determined for a particular lithology and receiver arrangement, quasi-real-time monitoring is feasible. While CWD inversion cannot provide the same spatial resolution as synchrotron microtomography, it appears to demonstrate similar sensitivity to the onset of microscopic inelastic strain.

There also exist considerable opportunity to improve upon the application CWD within the laboratory setting. In terms of the application of the theory, the most pressing area where improvements can be made are the sensitivity kernels used in this study (Equation 2). As previously mentioned these do not account for the core boundaries, any in situ heterogeneities, or the anisotropic layered nature of the WMF as they assume the source-receiver pairs are placed within an infinite, isotropic medium. Several works have proposed to better account for the initial material state by first determining the sensitivity kernels through numerically modeling of the propagation of energy within (Kanu & Snieder, 2015; Xue et al., 2019). By doing so, one would no longer be restricted to the use of information (time windows) within the coda, as the sensitivity kernels of the coherent arrivals would also be known. Such a numerical study would also provide insight into another limitation of the current application of CWD, namely the inability to clearly discern between a region undergoing localized microscopic change and one undergoing macroscopic change. In other words, a numerical analysis would allow for the assessment of the spatial resolution to change within a particular lithology and acquisition parameters.

5. Conclusion

The CWD inversion monitoring of the Whitby Mudstone during triaxial compaction indicates that the formation of inelastic strain localization occurs at less than 42% of peak stress. The absence of the detection of any AEs suggests such inelastic localizations develop gradually, not impulsively, from microscopic diffuse damage, up until the macroscopic shear failure, while the comparison of different S_w suggests a nonlinear relationship with the onset of strain localization. In general, the application of CWD inversion to what is ostensibly an aseismic mudstone has enabled a qualitative discussion of the time and location at which initial microscopic inelastic strain (opening, closure, and shearing) develops. Furthermore, subsequent stages of reactivation and eventual macroscopic shear failure are discernible.

Appendix A: The Least Squares Inversion Scheme

The following details the exact implementation of the least squares formulation used within this study, which itself follows the structure of implementation presented by Planès et al. (2015). Here the formulation proposed by (Tarantola, 2005; Valette & Tarantola, 1982) is applied in order to invert for estimated model parameters \mathbf{m} . The least squares misfit function $S(\mathbf{m})$ is given as

$$S(\mathbf{m}) = \|\mathbf{G}\mathbf{m} - \mathbf{K}_p^m\|_D^2 + \|\mathbf{m} - \mathbf{m}_{prior}\|_M^2, \quad (\text{A1})$$

where $\|\cdot\|_D^2$ is the l_2 norm of the data weighted by its covariance matrix \mathbf{C}_D^{-1} , and $\|\cdot\|_M^2$ is the l_2 norm of the model weighted by its covariance matrix \mathbf{C}_M^{-1} . Here the term $\|\cdot\|_D^2$ measures the distance between the estimated model and the measured decorrelation coefficients \mathbf{K}_p^m while $\|\cdot\|_M^2$ measures the distance between the estimated model and any prior information held within \mathbf{m}_{prior} . The explicit solution which minimizes this cost function is given by Tarantola (2005) as

$$\hat{\mathbf{m}} = \mathbf{m}_{prior} + (\mathbf{G}^T \mathbf{C}_D^{-1} \mathbf{G} + \mathbf{C}_M^{-1})^{-1} \mathbf{G}^T \mathbf{C}_D^{-1} (\mathbf{K}_p^m - \mathbf{G}\mathbf{m}_{prior}). \quad (\text{A2})$$

In terms of the misfit function Equation A1, from which Equation A2 is derived, the construction of \mathbf{C}_D and \mathbf{C}_M allows the tuning of our confidence in the measured data and the a priori model, respectively. Here we make the choice of defining \mathbf{C}_D as a diagonal matrix, thereby neglecting the correlations between different measurement pairs and nonoverlapping time windows. The relative error for all measurement pairs and nonoverlapping time windows is estimated from the observed fluctuation between neighboring time windows as $\sim 30\%$. That said, when considering Equation A1 it is evident that the relative weight of \mathbf{C}_D and \mathbf{C}_M is what controls the achievable $S(\mathbf{m})$ and therefore the magnitude of the diagonal of \mathbf{C}_D are arbitrary. The elements of \mathbf{C}_D are therefore constructed as

$$C_{Dij} = \left(0, 3K_{p_i}^m\right)^2 \delta_{ij}, \quad (\text{A3})$$

where δ_{ij} is the Kronecker delta and $K_{p_i}^m$ is the measurement i acquired during survey p . The model covariance matrix \mathbf{C}_M is defined through an exponential correlation between the model cells (Froment, 2011) in an effort to reduce the underdetermined nature of the problem (i.e., many more tetrahedra than measurements).

$$C_{Mij} = \left(\sigma_m \frac{L_0}{L_c}\right)^2 e^{-\|r_i - r_j\|/L_c}, \quad (\text{A4})$$

where σ_m defines the standard deviation from the a priori model, while L_0 corresponds to the size of the model cells (tetrahedra) which discretize the core sample, and L_c controls the correlation distance between cells at positions r_i and r_j . The L-curve method (Hansen, 1992) is applied to the \mathbf{D}_p pertaining to each core sample, at a single survey time p , in order to tune the free parameters σ_m and L_c in search of a global optimum across all core samples. This optimum is found by a trade-off between the fit of the data $\|\mathbf{K}_p^m - \mathbf{G}\hat{\mathbf{m}}\|$ and the norm of the estimated model $\hat{\mathbf{m}}$. Through this process we arrive at $\sigma_m = 0.53$ and $L_c = 12.26$, values which are held constant throughout this study.

During the inversion procedure at each time step/survey p a positivity constrain is imposed on σ_{T_p} through an iterative procedure, where any negative $\tilde{\mathbf{m}}$ are set to zero until convergence is achieved, typically requiring $n \leq 10$ iterations. To achieve this the inversion algorithm in Equation A2 is modified with a recursive update for n iterations as

$$\tilde{\mathbf{m}}^{n+1} = \tilde{\mathbf{m}}_{prior}^n + (\mathbf{G}^T \mathbf{C}_D^{-1} \mathbf{G} + \mathbf{C}_M^{n-1})^{-1} \mathbf{G}^T \mathbf{C}_D^{-1} (\mathbf{K}_p^m - \mathbf{G} \tilde{\mathbf{m}}_{prior}^n), \quad (\text{A5})$$

where $\tilde{\mathbf{m}}_{prior}^n$ is the estimated distribution of σ_{T_p} at iteration n after setting negative values to zero, while the update of the model covariance matrix is determined as

$$\tilde{\mathbf{C}}_M^n = (\mathbf{G}^T \mathbf{C}_D^{-1} \mathbf{G} + \mathbf{C}_M^{n-1})^{-1}. \quad (\text{A6})$$

The initial m_{prior} are set to zero at the beginning of this recursive update of $\tilde{\mathbf{m}}$. This ensures each time step p is independent from one another, and therefore, any observed correlations between successive distributions of σ_{T_p} are derived from the input data \mathbf{K}_p^m .

Data Availability Statement

The raw acoustic and mechanical data used in this study are available at Zotz-Wilson, Douma, et al. (2019), under the name “Acoustic, mechanical, and microstructure data used in: Ultrasonic Imaging of the Onset and Growth of Fractures within Partially Saturated Whitby Mudstone using Coda-Wave Decorrelation Inversion.”

Acknowledgments

We would like to thank David Nguyen and Stephen Firms at CSIRO's Geomechanics and Geophysics Laboratory for their assistance during the experimentation. The assistance provided by Joost Van Meel at TUDelft in postprocessing the CT-scans is also much appreciated. Further, the funding provided by the Dutch Upstream Gas top-sector initiative (project TKIG01020) and our industry partners Energie Beheer Nederland B.V., and Neptune Energy Netherlands B.V., Wintershall Noordzee B.V. is acknowledged. Furthermore, we would like to acknowledge the use of the open-source python module pyVista (Sullivan & Kaszynski, 2019), which is used to visualize all of the 3-D fracture networks and CWD inversion results.

References

- Aben, F. M., Brantut, N., Mitchell, T. M., & David, E. C. (2019). Rupture energetics in crustal rock from laboratory-scale seismic tomography. *Geophysical Research Letters*, *46*, 7337–7344. <https://doi.org/10.1029/2019GL083040>
- Aik T., & Sundell, R. (2014). ONKALO—From concept to reality. 1, pp. 1–9, WM2014 Conference, Phoenix.
- Anugonda, P., Wiehn, J. S., & Turner, J. A. (2001). Diffusion of ultrasound in concrete. *Ultrasonics*, *39*(6), 429–435. [https://doi.org/10.1016/S0041-624X\(01\)00077-4](https://doi.org/10.1016/S0041-624X(01)00077-4)
- Aplin, A. C., & Macquaker, J. H. (2011). Mudstone diversity: Origin and implications for source, seal, and reservoir properties in petroleum systems. *American Association of Petroleum Geologists Bulletin*, *95*, 2031–2059. <https://doi.org/10.1306/03281110162>
- Armitage, P. J., Worden, R. H., Faulkner, D. R., Butcher, A. R., & Espie, A. A. (2016). Permeability of the Mercia Mudstone: Suitability as caprock to carbon capture and storage sites. *Geofluids*, *16*(1), 26–42. <https://doi.org/10.1111/gfl.12134>
- Ayalew, L., & Yamagishi, H. (2005). The application of GIS-based logistic regression for landslide susceptibility mapping in the Kakuda-Yahiko Mountains, Central Japan. *Geomorphology*, *65*(1-2), 15–31. <https://doi.org/10.1016/j.geomorph.2004.06.010>
- Brantut, N. (2018). Time-resolved tomography using acoustic emissions in the laboratory, and application to sandstone compaction. *Geophysical Journal International*, *213*, 2177–2192. <https://doi.org/10.1093/gji/ggy068>
- Brookins, D. G. (1976). Shale as a repository for radioactive waste: The evidence from Oklo. *Environmental Geology*, *1*(5), 255–259. <https://doi.org/10.1007/BF02676715>
- Busch, A., Alles, S., Gensterblum, Y., Prinz, D., Dewhurst, D., Raven, M., et al. (2008). Carbon dioxide storage potential of shales. *International Journal of Greenhouse Gas Control*, *2*(3), 297–308. <https://doi.org/10.1016/j.ijggc.2008.03.003>
- Crank, J. (1975). *The mathematics of diffusion* (2nd ed., Vol. 5, pp. 1267–1268). Oxford: Oxford University Press. <https://doi.org/10.1021/ja01562a072>
- Dewhurst, D. N., Sarout, J., Delle Piane, C., Siggins, A. F., & Raven, M. D. (2015). Empirical strength prediction for preserved shales. *Marine Petroleum Geology*, *67*, 512–525. <https://doi.org/10.1016/j.marpetgeo.2015.06.004>
- Douma, L. A. N. R., Dautriat, J., Sarout, J., Dewhurst, D. N., & Barnhoorn, A. (2019). Impact of water saturation on the elastic anisotropy of the Whitby Mudstone. United Kingdom, Submitt. to Geophys.
- Ewy, R. T. (2014). Shale swelling/shrinkage and water content change due to imposed suction and due to direct brine contact. *Acta Geotechnica*, *9*(5), 869–886. <https://doi.org/10.1007/s11440-013-0297-5>
- Ferrari, A., Favero, V., Marschall, P., & Laloui, L. (2014). Experimental analysis of the water retention behaviour of shales. *International Journal of Rock Mechanics and Mining Science*, *72*, 61–70. <https://doi.org/10.1016/j.ijrmm.2014.08.011>
- Fjær, E., Holt, R., Raaen, A. M., Risnes, R., & Horsrud, P. (2008). *Petroleum related rock mechanics* (2nd ed., pp. 251–287). Netherlands: Elsevier Science.
- Forsans, T. M., & Schmitt, L. (1994). Capillary forces: The neglected factor in shale instability studies? *Society of Petroleum Engineers - Rock Mechanics in Petroleum Engineering*, *1994*, 71–84.
- Froment, B. (2011). Monitoring slight mechanical changes using seismic background noise (PhD thesis), University of Grenoble.
- Garrels, R. M., & Mackenzie, F. T. (1969). Sedimentary rock types: Relative proportions as a function of geological time. *Science* (80-), *163*(3867), 570–571. <https://doi.org/10.1126/science.163.3867.570>
- Getis, A., & Ord, J. K. (2010). The analysis of spatial association by use of distance statistics. In L. Anselin, & S. Rey (Eds.), *Advances spatial science*. Berlin: Springer. https://doi.org/10.1007/978-3-642-01976-0_10
- Geuzaine, C., & Remacle, J.-F. (2017). A three-dimensional finite element mesh generator with built-in pre- and post-processing facilities. *International Journal Numerical Methods Engineering*, *11*, 79.

- Ghorbani, A., Zamora, M., & Cosenza, P. (2009). Effects of desiccation on the elastic wave velocities of clay-rocks. *International Journal of Rock Mechanics and Mining Science*, *46*(8), 1267–1272. <https://doi.org/10.1016/j.ijrmmms.2009.01.009>
- Grêt, A. (2005). Monitoring rapid temporal change in a volcano with coda wave interferometry. *Geophysical Research Letters*, *32*, L06304. <https://doi.org/10.1029/2004GL021143>
- Grêt, A., Snieder, R., & Özbay, U. (2006a). Monitoring in situ stress changes in a mining environment with coda wave interferometry. *Geophysical Journal International*, *167*(2), 504–508. <https://doi.org/10.1111/j.1365-246X.2006.03097.x>
- Grêt, A., Snieder, R., & Scales, J. (2006b). Time-lapse monitoring of rock properties with coda wave interferometry. *Journal of Geophysical Research*, *111*, B03305. <https://doi.org/10.1029/2004JB003354>
- Griffiths, L., Lengliné, O., Heap, M. J., Baud, P., & Schmittbuhl, J. (2018). Thermal cracking in Westerly Granite monitored using direct wave velocity, coda wave interferometry, and acoustic emissions. *Journal of Geophysical Research: Solid Earth*, *123*, 2246–2261. <https://doi.org/10.1002/2017JB015191>
- Hansen, P. C. (1992). Analysis of discrete ill-posed problems by means of the *L*-curve. *SIAM Review*, *34*(4), 561–580. <https://doi.org/10.1137/1034115>
- Heap, M. J., Baud, P., Meredith, P. G., Bell, A. F., & Main, I. G. (2009). Time-dependent brittle creep in Darley Dale sandstone. *Journal of Geophysical Research*, *114*, B07203. <https://doi.org/10.1029/2008JB006212>
- Houben, M. E., Barnhoorn, A., Lie-A-Fat, J., Ravestein, T., Peach, C. J., & Drury, M. R. (2016). Microstructural characteristics of the Whitby Mudstone Formation (UK). *Mar Petroleum Geology*, *70*, 185–200. <https://doi.org/10.1016/j.marpetgeo.2015.11.011>
- Houben, M. E., Barnhoorn, A., Wasch, L., Trabucho-Alexandre, J., Peach, C., & Drury, M. (2016). Microstructures of Early Jurassic (Toarcian) shales of northern Europe. *International Journal of Coal Geology*, *165*, 76–89. <https://doi.org/10.1016/j.coal.2016.08.003>
- Izumi, K., Ogihara, M., & Kameyaf, H. (1998). Displacements of bridge foundations on sedimentary soft rock: A case study on small-strain stiffness. *Géotechnique*, *47*, 233–246. <https://doi.org/10.1680/jpbog.26421.0016>
- Jansen, D. P., Carlson, S. R., Young, R. P., & Hutchins, D. A. (1993). Ultrasonic imaging and acoustic emission monitoring of thermally induced microcracks in Lac du Bonnet granite. *Journal of Geophysical Research*, *98*(B12), 22,231–22,243.
- Jianghui, M., Min, Z., Hongjing, Z., Luofu, L., Zhiyong, W., Jieli, Z., & Ying, W. (2012). Geochemical evidence for coal and carbonaceous mudstone as the possible major oil source rock in the Jurassic Turpan Basin, northwest China. *Acta Geologica Sinica - English Editor*, *86*(5), 1171–1181. <https://doi.org/10.1111/j.1755-6724.2012.00739.x>
- Kandula, N., Cordonnier, B., Dysthe, D. K., Sanchez, J. R., Zheng, X., Renard, F., et al. (2018). Dynamic in situ three-dimensional imaging and digital volume correlation analysis to quantify strain localization and fracture coalescence in sandstone. *Pure and Applied Geophysics*, *176*, 1083–1115. <https://doi.org/10.1007/s00024-018-2003-x>
- Kanu, C., & Snieder, R. (2015). Numerical computation of the sensitivity kernel for monitoring weak changes with multiply scattered acoustic waves. *Geophysical Journal International*, *203*(3), 1923–1936. <https://doi.org/10.1093/gji/ggv391>
- Laloui, L., Salager, S., & Rizzi, M. (2013). *Retention behaviour of natural clayey materials at different temperatures* (Vol. 8, pp. 537–546). <https://doi.org/10.1007/s11440-013-0255-2>
- Larose, E., De Rosny, J., Margerin, L., Anache, D., Gouedard, P., Campillo, M., & Van Tiggelen, B. (2006). Observation of multiple scattering of kHz vibrations in a concrete structure and application to monitoring weak changes. *Physical Review E: Statistical, Nonlinear, and Soft Matter Physics*, *76*, 016609. <https://doi.org/10.1103/PhysRevE.73.016609>
- Larose, E., & Hall, S. (2009). Monitoring stress related velocity variation in concrete with a 2E10-5 relative resolution using diffuse ultrasound. *The Journal of the Acoustical Society of America*, *125*(4), 1853–1856. <https://doi.org/10.1121/1.3079771>
- Larose, E., Obermann, A., Digulescu, A., Planès, T., Chaix, J.-F., Mazerolle, F., & Moreau, G. (2015). Locating and characterizing a crack in concrete with diffuse ultrasound: A four-point bending test. *The Journal of the Acoustical Society of America*, *138*(1), 232–241. <https://doi.org/10.1121/1.4922330>
- Larose, E., Planes, T., Rossetto, V., & Margerin, L. (2010). Locating a small change in a multiple scattering environment. *Applied Physics Letters*, *96*(20), 204,101. <https://doi.org/10.1063/1.3431269>
- Lei, X., Masuda, K., Nishizawa, O., Jouniaux, L., Liu, L., Ma, W., et al. (2004). Detailed analysis of acoustic emission activity during cataclastic fracture of faults in rock. *Journal of Structural Geology*, *26*(2), 247–258. [https://doi.org/10.1016/S0191-8141\(03\)00095-6](https://doi.org/10.1016/S0191-8141(03)00095-6)
- Linnaeus, C. (1771). *Mantissa plantarum*. Mantissa plant.
- Lockner, D. (1993). The role of acoustic emission in the study of rock fracture. *International Journal of Rock Mechanics and Mining Science and Geomechanics Abstracts*, *30*(7), 883–899. [https://doi.org/10.1016/0148-9062\(93\)90041-B](https://doi.org/10.1016/0148-9062(93)90041-B)
- Lockner, D. A., Walsh, J. B., & Byerlee, J. D. (1977). Changes in seismic velocity and attenuation during deformation of granite. *Journal of Geophysical Research*, *82*(33), 5374–5378. <https://doi.org/10.1029/JB082i033p05374>
- Main, I. G. (1990). Quasi-static modelling of stress histories during the earthquake cycle: Precursory seismic and aseismic stress release. *Geophysical Journal International*, *102*(1), 195–203. <https://doi.org/10.1111/j.1365-246X.1990.tb00541.x>
- Mao, L., & Chiang, F.-P. (2016). 3D strain mapping in rocks using digital volumetric speckle photography technique. *Acta Mechanica*, *227*(11), 3069–3085. <https://doi.org/10.1007/s00707-015-1531-z>
- Mao, L., Liu, H., Zhu, Y., Zhu, Z., Guo, R., & Chiang, F.-P. (2019). 3D strain mapping of opaque materials using an improved digital volumetric speckle photography technique with X-ray microtomography. *Applied Sciences*, *9*(7), 1418. <https://doi.org/10.3390/app9071418>
- McBeck, J., Kobchenko, M., Hall, S. A., Tudisco, E., Cordonnier, B., Meakin, P., & Renard, F. (2018). Investigating the onset of strain localization within anisotropic shale using digital volume correlation of time-resolved X-ray microtomography images. *Journal of Geophysical Research: Solid Earth*, *123*, 7509–7528. <https://doi.org/10.1029/2018JB015676>
- Obermann, A., Froment, B., Campillo, M., Larose, E., Planès, T., Valette, B., et al. (2014). Seismic noise correlations to image structural and mechanical changes associated with the Mw 7.9 2008 Wenchuan earthquake. *Journal of Geophysical Research: Solid Earth*, *119*, 3155–3168. <https://doi.org/10.1002/2013JB010932>. Received
- Obermann, A., Planès, T., Larose, E., & Campillo, M. (2013). Imaging preruptive and coeruptive structural and mechanical changes of a volcano with ambient seismic noise. *Journal of Geophysical Research: Solid Earth*, *118*, 6285–6294. <https://doi.org/10.1002/2013JB010399>
- Obermann, A., Planès, T., Larose, E., & Campillo, M. (2019). 4-D imaging of subsurface changes with coda waves: Numerical studies of 3-D combined sensitivity kernels and applications to the M_w 7.9, 2008 Wenchuan earthquake. *Pure and Applied Geophysics*, *176*(3), 1243–1254. <https://doi.org/10.1007/s00024-018-2014-7>
- Onaisi, A., Durand, C., & Audibert, A. (1994). Role of hydration state of shales in borehole stability studies. *Society of Petroleum Engineers - Rock Mech. Pet. Eng.*, *1994*, 275–285.

- Paterson, M. S., & Wong, T. F. (2005). Experimental rock deformation—The brittle field, *Exp. rock deform.—Brittle F* (pp. 32). Berlin/Heidelberg: Springer-Verlag. <https://doi.org/10.1007/b137431>
- Payan, C., Garnier, V., Moysan, J., & Johnson, P. A. (2009). Determination of third order elastic constants in a complex solid applying coda wave interferometry. *Applied Physics Letters*, *94*, 011904. <https://doi.org/10.1063/1.3064129>
- Peng, J., & Yang, S. Q. (2018). Comparison of mechanical behavior and acoustic emission characteristics of three thermally-damaged rocks. *Energies*, *11*(9), 2350. <https://doi.org/10.3390/en11092350>
- Planès, T., Larose, E., Rossetto, V., & Margerin, L. (2015). Imaging multiple local changes in heterogeneous media with diffuse waves. *The Journal of the Acoustical Society of America*, *137*(2), 660–667. <https://doi.org/10.1121/1.4906824>
- Powell, J. H. (2010). Jurassic sedimentation in the Cleveland Basin: A review. *Proceedings of the Yorkshire Geological Society*, *58*(1), 21–72. <https://doi.org/10.1144/pygs.58.1.278>
- Pye, K. (1985). Electron microscope analysis of zoned dolomite rhombs in the Jet Rock Formation (Lower Toarcian) of the Whitby area, U.K. *Geological Magazine*, *122*(3), 279–286. <https://doi.org/10.1017/S0016756800031496>
- Ramos da Silva, M., Schroeder, C., & Verbrugge, J. C. (2008). Unsaturated rock mechanics applied to a low-porosity shale. *Engineering Geology*, *97*(1–2), 42–52. <https://doi.org/10.1016/j.enggeo.2007.12.003>
- Renard, F., Cordonnier, B., Kobchenko, M., Kandula, N., Weiss, J., & Zhu, W. (2017). Microscale characterization of rupture nucleation unravels precursors to faulting in rocks. *Earth Planet Science Letters*, *476*, 69–78. <https://doi.org/10.1016/j.epsl.2017.08.002>
- Renard, F., Weiss, J., Mathiesen, J., Ben-Zion, Y., Kandula, N., & Cordonnier, B. (2018). Critical evolution of damage toward system-size failure in crystalline rock. *Journal of Geophysical Research: Solid Earth*, *123*, 1969–1986. <https://doi.org/10.1002/2017JB014964>
- Rey, S. J., & Anselin, L. (2007). PySAL: A Python library of spatial analytical methods. *Review of Regional Studies*, *37*, 5–27. https://doi.org/10.1007/978-3-642-03647-7_11
- Robinson, D. J., Sambridge, M., & Snieder, R. (2007). Constraints on coda wave interferometry estimates of source separation: The acoustic case. *Exploration Geophysics*, *38*, 189–199. <https://doi.org/10.1071/EG07019>
- Robinson, D. J., Snieder, R., & Sambridge, M. (2007). Using coda wave interferometry for estimating the variation in source mechanism between double couple events. *Journal of Geophysical Research*, *112*, B12302. <https://doi.org/10.1029/2007JB004925>
- Rossetto, V., Margerin, L., Planès, T., & Larose, E. (2011). Locating a weak change using diffuse waves: Theoretical approach and inversion procedure. *Journal of Applied Physics*, *109*(3), 034903. <https://doi.org/10.1063/1.3544503>
- Salvermoser, J., Hadziioannou, C., & Staehler, S. C. (2015). Structural monitoring of a highway bridge using passive noise recordings from street traffic. *The Journal of the Acoustical Society of America*, *138*(6), 3864–3872. <https://doi.org/10.1121/1.4937765>
- Sarout, J., Delle Piane, C., Nadri, D., Esteban, L., & Dewhurst, D. N. (2015). A robust experimental determination of Thomsen's δ parameter. *Geophysics*, *80*(1), A19–A24. <https://doi.org/10.1190/geo2014-0391.1>
- Sarout, J., Le Gonidec, Y., Ougier-Simonin, A., Schubnel, A., Gueguen, Y., & Dewhurst, D. N. (2017). Laboratory micro-seismic signature of shear faulting and fault slip in shale. *Physics of the Earth and Planetary Interiors*, *264*, 47–62. <https://doi.org/10.1016/j.pepi.2016.11.005>
- Sens-Schönfelder, C., & Larose, E. (2008). Temporal changes in the lunar soil from correlation of diffuse vibrations. *Physical Review E: Statistical, Nonlinear, and Soft Matter Physics*, *78*(4), 1–4. <https://doi.org/10.1103/PhysRevE.78.045601>
- Sens-Schönfelder, C., & Wegler, U. (2006). Passive image interferometry and seasonal variations of seismic velocities at Merapi Volcano, Indonesia. *Geophysical Research Letters*, *33*, L21302. <https://doi.org/10.1029/2006GL027797>
- Singh, J., Curtis, A., Zhao, Y., Cartwright-Taylor, A., & Main, I. (2019). *Journal of Geophysical Research: Solid Earth*, *124*, 5629–5655. <https://doi.org/10.1029/2019JB017577>
- Snieder, R. (2002). Coda wave interferometry for estimating nonlinear behavior in seismic velocity. *Science* (80-.), *295*(5663), 2253–2255. <https://doi.org/10.1126/science.1070015>
- Snieder, R., & Hagerty, M. (2004). Monitoring change in volcanic interiors using coda wave interferometry: Application to Arenal Volcano, Costa Rica. *Geophysical Research Letters*, *31*, L09608. <https://doi.org/10.1029/2004GL019670>
- Sullivan, C., & Kaszynski, A. (2019). PyVista: 3D plotting and mesh analysis through a streamlined interface for the Visualization Toolkit (VTK). *Journal of Open Source Software*, *4*(37), 1450. <https://doi.org/10.21105/joss.01450>
- Tarantola, A. (2005). Inverse problem theory and methods for model parameter estimation, *Society for Industrial and Applied Mathematics* (Vol. 120, pp. 1816–24). <https://doi.org/10.1137/1.9780898717921>
- Vales, F., Nguyen Minh, D., Gharbi, H., & Rejeb, A. (2004). Experimental study of the influence of the degree of saturation on physical and mechanical properties in Tournemire shale (France), *Appl. Clay Science*, *26*(1–4 SPEC. ISS.), 197–207. <https://doi.org/10.1016/j.clay.2003.12.032>
- Valette, B., & Tarantola, A. (1982). Generalized nonlinear inverse problems solved using the least squares criterion. *Reviews of Geophysics*, *20*(2), 219.
- Vomvoris, S., Claudel, A., Blechschmidt, I., & Muller, H. (2013). The Swiss Radioactive Waste Management Program—Brief history, status, and outlook. *Journal of Nuclear Fuel Cycle and Waste Technology*, *1*(1), 9–27. <https://doi.org/10.7733/jnfcwt.2013.1.1.9>
- Wang, T., Wu, H., Li, Y., Gui, H., Zhou, Y., Chen, M., et al. (2013). Stability analysis of the slope around flood discharge tunnel under inner water exosmosis at Yangqu hydropower station. *Computers and Geotechnics*, *51*, 1–11. <https://doi.org/10.1016/j.compgeo.2013.01.006>
- Weaver, R. L., & Lobkis, O. I. (2000). Temperature dependence of diffuse field phase. *Ultrasonics*, *38*, 491–494. [https://doi.org/10.1016/S0041-624X\(99\)00047-5](https://doi.org/10.1016/S0041-624X(99)00047-5)
- Xue, Q., Larose, E., & Moreau, L. (2019). Locating structural changes in a multiple scattering domain with an irregular shape. *The Journal of the Acoustical Society of America*, *146*(1), 595–602. <https://doi.org/10.1121/1.5118246>
- Yoshida, N., Nishi, M., Kitamura, M., & Adachi, T. (1997). Analysis of mudstone deterioration and its effect on tunnel performance. *International Journal of Rock Mechanics and Mining Sciences*, *34*(3–4), 353.e1–353.e19. [https://doi.org/10.1016/S1365-1609\(97\)00289-X](https://doi.org/10.1016/S1365-1609(97)00289-X)
- Zhan, H., Jiang, H., & Jiang, R. (2020). Three-dimensional images generated from diffuse ultrasound wave: Detections of multiple cracks in concrete structures. *Structural Health Monitoring*, *19*(1), 12–25. <https://doi.org/10.1177/1475921719834045>
- Zhang, Y., Abraham, O., Grondin, F., Loukili, A., Tournat, V., Duff, A. L., et al. (2012). Study of stress-induced velocity variation in concrete under direct tensile force and monitoring of the damage level by using thermally-compensated coda wave interferometry. *Ultrasonics*, *52*(8), 1038–1045. <https://doi.org/10.1016/j.ultras.2012.08.011>
- Zhang, Y., Abraham, O., Tournat, V., Le Duff, A., Lascoup, B., Loukili, A., et al. (2013). Validation of a thermal bias control technique for coda wave interferometry (CWI). *Ultrasonics*, *53*(3), 658–664. <https://doi.org/10.1016/j.ultras.2012.08.003>
- Zhang, Y., Larose, E., Moreau, L., & D'Ozouville, G. (2018). Three-dimensional in-situ imaging of cracks in concrete using diffuse ultrasound. *Structural Health Monitoring*, *17*(2), 279–284. <https://doi.org/10.1177/1475921717690938>

- Zhang, Y., Planès, T., Larose, E., Obermann, A., Rospars, C., & Moreau, G. (2016). Diffuse ultrasound monitoring of stress and damage development on a 15-ton concrete beam. *The Journal of the Acoustical Society of America*, *139*(4), 1691–1701. <https://doi.org/10.1121/1.4945097>
- Zijp, M., Ten Veen, J., Verreussel, R., Heege, J. T., Ventra, D., & Martin, J. (2015). Shale gas formation research: From well logs to outcrop—And back again. *First Break*, *33*(2), 99–106.
- Zotz-Wilson, R. (2019). Coda-Analysis: First release of Coda-Analysis. <https://doi.org/10.5281/zenodo.3255940>
- Zotz-Wilson, R., Boerrigter, T., & Barnhoorn, A. (2019). Coda-wave monitoring of continuously evolving material properties and the precursory detection of yielding. *The Journal of the Acoustical Society of America*, *145*(2), 1060–1068. <https://doi.org/10.1121/1.5091012>
- Zotz-Wilson, R., Douma, L. A. N. R., Sarout, J., Dautriat, J., Dewhurst, D. N., & Barnhoorn, A. (2019). Ultrasonic imaging of the onset and growth of fractures within partially saturated Whitby Mudstone using coda-wave decorrelation inversion. <https://doi.org/10.4121/uuid:dc3627dd-8434-4fa3-a4f0-b886c31c1ce2>